ARTIFICIAL NEURON USING MoS_2/GRAPHENE THRESHOLD SWITCHING MEMRISTOR

by

HIROKJYOTI KALITA

B.Tech. SRM University, 2015

A thesis submitted in partial fulfilment of the requirements
for the degree of Master of Science
in the Department of Electrical and Computer Engineering
in the College of Engineering and Computer Science
at the University of Central Florida
Orlando, Florida

Summer Term
2018

Major Professor: Tania Roy

ABSTRACT

With the ever-increasing demand for low power electronics, neuromorphic computing has garnered huge interest in recent times. Implementing neuromorphic computing in hardware will be a severe boost for applications involving complex processes such as pattern recognition. Artificial neurons form a critical part in neuromorphic circuits, and have been realized with complex complementary metal–oxide–semiconductor (CMOS) circuitry in the past. Recently, insulator-to-metal-transition (IMT) materials have been used to realize artificial neurons. Although memristors have been implemented to realize synaptic behavior, not much work has been reported regarding the neuronal response achieved with these devices. In this work, we study the IMT in 1T-TaS_2 and the volatile threshold switching behavior in vertical-MoS_2 (v-MoS_2) and graphene van der Waals heterojunction system. The v-MoS_2/graphene threshold switching memristor (TSM) is used to produce the integrate-and-fire response of a neuron. We use large area chemical vapor deposited (CVD) graphene and MoS_2, enabling large scale realization of these devices. These devices can emulate the most vital properties of a neuron, including the all or nothing spiking, the threshold driven spiking of the action potential, the post-firing refractory period of a neuron and strength modulated frequency response. These results show that the developed artificial neuron can play a crucial role in neuromorphic computing.

ACKNOWLEDGMENT

First and foremost, I would like to express my sincere gratitude to my advisor Dr. Tania Roy for her encouragement, excellent guidance, and involvement throughout my thesis. She has always believed in my abilities and this thesis would not have been complete without her support.

I would also like to thank Dr. Jiann S. Yuan and Dr. Kalpathy Sundaram for providing me with intellectual insights on the research.

I am extremely grateful to our research group at University of Central Florida - Adithi Krishnaprasad, Dr. Sonali Das, Durjoy Dev and Dr. Nitin Choudhary. I would like to thank Adithi for her immense help with all the fabrication work in the cleanroom. I am ever thankful to Sonali and Durjoy for their valuable insight in the design work and for all the stimulating discussions which have helped me gain insights in the research and guiding me in writing this thesis. My heartfelt gratitude to Nitin for helping me with the growth of MoS_2. I would also like to thank Yi Ding for helping me with the Raman measurements.

Last but not the least, I would like to thank my parents, grandparents and Devika for their constant support throughout the period.

TABLE OF CONTENTS

LIST OF FIGURES

CHAPTER 1 : INTRODUCTION

1.1 Overview

Understanding the complex and overwhelming functioning of the human brain has always fascinated scientists and researchers for biological fields and beyond. The way the human brain can process huge amounts of data and handle pattern recognition with relative ease is immensely compelling and its complexity is continuously evolving. The building blocks in the brain consist of interconnected neurons and synapses, which cooperate efficiently to process incoming signals and decide on outgoing actions. The schematic of a biological neuron connected to multiple synapses is shown in Figure 1.

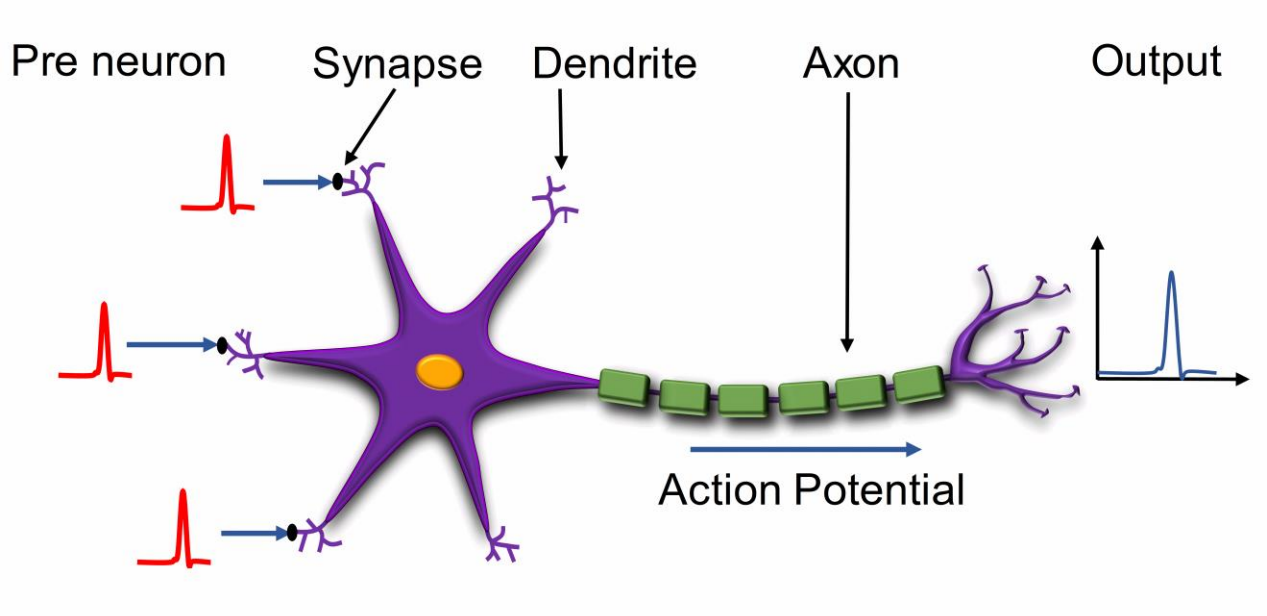

Figure 1. Schematic of a biological neuron connected to other neurons through synapses

A biological neuron is connected to several other neurons through connections known as synapses. Depending upon the input signals received by the dendrites, an action potential (also

referred to as a neuron spike) is generated by the soma of the neuron which is then passed by the axon to other neurons through synapses. The electrical equilibrium is maintained by the movement of various ions such as Na^+, K^+, Cl^- and Ca^{2+} in and out of the neuron cell. The potential difference between the interior and the exterior of the neuron is referred to as the membrane potential[1]. As the membrane potential starts building up and rises beyond a particular threshold voltage, the neuron produces an output spike[2, 3]. This phenomenon of neuron spiking is shown in Figure 2. The neuron does not fire immediately after producing a spike even if it keeps receiving input signals. This period is known as the refractory period of a neuron[4, 5]. After the refractory period, the neuron starts integrating the input again and prepares for another spike.

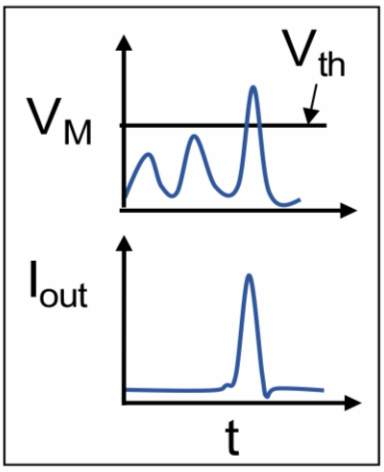

Figure 2. Artificial neuron spiking as a function of the membrane potential

1.2 Artificial Neural Network

Inspired by the operation of the human brain, various neuromorphic devices, circuits, and systems have been developed that can work analogous to the brain. Owing to the low power

dissipation and characteristics that are similar to biological neurons, spiking neural networks (SNN) have garnered huge interests for mimicking and closely resembling the neuro-biological system[1]. SNNs, the third generation of neural network models, have been found to be more hardware friendly and energy efficient; thus making them more biologically realistic compared to other neural networks[6]. The key components of an SNN are artificial neurons and synapses where the synapses connect the pre-neurons and the post-neurons. SNN uses discrete rather than continuous spikes along with the incorporation of the concept of time. It involves efficient transfer of information based on precise timing of a sequence of spikes. Important synaptic behaviors such as synaptic plasticity, long term potentiation and depression (LTP and LTD), and Spike Time dependent Plasticity (STDP) have been studied using emerging devices such as memristors for information processing, pattern recognition and learning methods of SNN[7-9], But, neuronal response has mostly been realized using complex CMOS circuitry[10, 11], which requires several transistors to mimic a single neuron. These circuits involve a large number of active components, increasing the power dissipation and making high density integration difficult[9, 11, 12], To overcome these issues, various emerging devices have been used to emulate a biological neuron behavior. Insulator to metal transition (IMT) in materials such as vanadium dioxide (VO_2)[4, 13] and niobium dioxide (NbO_2)[14], chalcogenide-based phase change materials[15], and magnetoelectric switching of ferromagnets such as bismuth ferrite ($BiFeO_3$)[1], have been considered to develop various types of artificial neurons. VO_2 has a very low critical temperature of ~340 K above which its switching behavior disappears, severely limiting the operational range of devices and making them unsuitable for on-chip integration[4, 13, 16]. In case of phase change materials-based neurons, the degree to which the neuronal

characteristics can be tuned with nominal circuitry is limited by the fact that switching properties arise from the physics of crystallization[15]. For the same reason, the switching speed in phase change neuron is slow. Threshold switching in memristors can be a natural choice for realizing artificial neurons. However, the exploitation of threshold switching in memristors to realize artificial neurons is relatively unexplored. Recently, a $Ag/SiO_2/Au$ threshold switching memristor (TSM) was used to demonstrate an integrate-and-fire neuron[17]. Figure 3 shows all the work that has been done to realize artificial neuron on a device level.

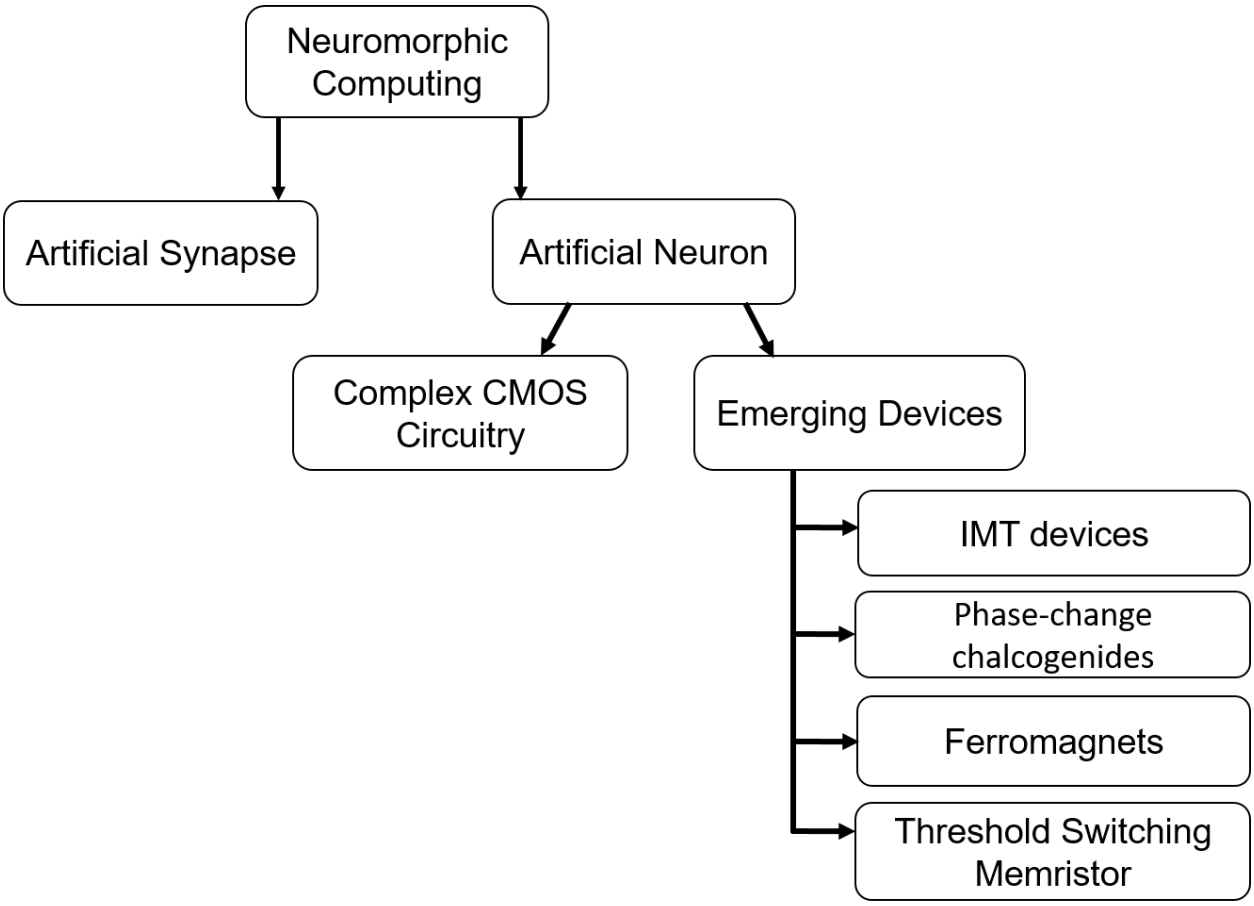

Figure 3. Previous work in realizing an artificial neuron

1.3 Two Dimensional Materials

The discovery of graphene in 2004 lead to a huge surge in the interest for two dimensional (2D) materials. Although graphene field-effect transistors (FETs) cannot be used for digital electronic applications because of its zero bandgap, it has led to a widespread increase in the interests in other 2D materials such as Transition Metal Dichalcogenides (TMDs). TMDs are a class of compound with a general formula MX_2 where M is Metal such as Mo, Sn, W etc. and X is a chalcogen such as S, Se, Te etc[18]. They form a unique class of compounds with almost 40 members already identified and possessing diverse properties. Most of the TMDs have a bandgap of about ~1-2eV for multilayers as well as for ultrathin monolayers. Also, since these 2D materials doesn't have any out of plane dangling bonds (shown in Figure 4) and are held together by van der Waal's forces, they can be easily stacked together giving a huge boost in terms increasing the integration density. TMDs can come in various forms for example: MoS_2, WS_2 and $MoSe_2$ are semiconductors, HfS_2 is an insulator, and NbS_2 and VSe_2 are true metals. The fact that these atomically thin sheets allow great thickness scalability along with high strength makes them viable for conventional semiconductor as well as for flexible electronics devices. Some TMDs such as $TaSe_2$, TaS_2, $TiSe_2$, $NbSe_2$ etc. show a phase transition property from a conducting state to a non-conducting state which will be discussed at length later.

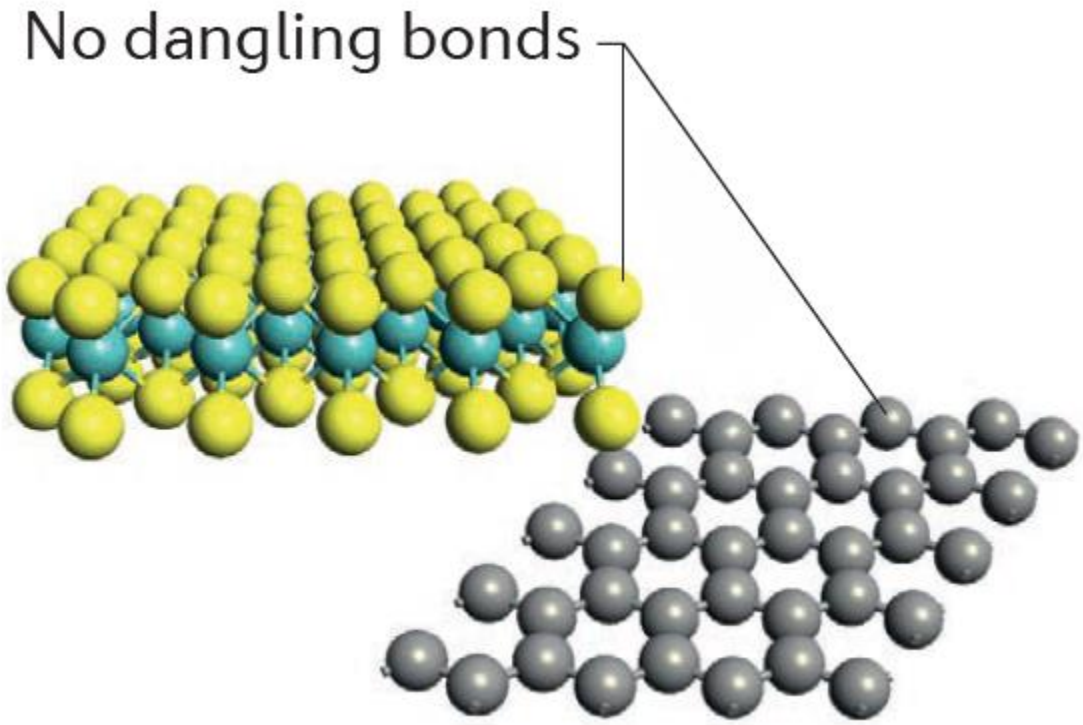

Figure 4. A pristine 2D material surface showing the absence of any dangling bonds[19]

Realizing an artificial neuron using 2D TMDs lead to better scalability for neuromorphic devices as well as bring them to the flexible platform. IMTs in materials such VO_2 and NbO_2 have been a popular platform for artificial neuron realization so, and hence we study the electrically driven IMT in 1T-TaS_2 for our work.

Large scale realization of field effect transistors (FETs) with 2D materials is limited by the unavailability of large area single-crystalline 2D materials. However, it has been reported that memristive properties can be obtained when polycrystalline films of Molybdenum disulfide (MoS_2) are used[20]. The volatile threshold switching observed in MoS_2 stimulates the

possibility of employing this phenomenon for the realization of artificial neurons. MoS_2 is one of most commonly studied TMDs because it is readily available in nature, have a bandgap of ~1.6eV (bulk MoS_2), and high quality 2D crystals can be relatively easily obtained. It is mechanically and chemically robust, and high quality flakes can be easily obtained by exfoliation. These varying properties provide a versatile platform for various electronic and optoelectronic devices using MoS_2[21]. However, observation of switching in lateral MoS_2 films mediated by the grain boundaries occludes scaling of lateral device dimensions. Hence, realizing such characteristics using a vertical structure can play a critical role in improving scaling opportunities.

1.4 Aim of the thesis

The aim of the thesis is to construct an artificial neuron using a complete 2D material system. Firstly, IMT in 1T-TaS_2 is explored for this purpose and then the volatile threshold switching in an all 2D/2D MoS_2/graphene heterojunction is studied in detail. By exploiting the threshold switching behavior in CVD-grown vertical MoS_2 (v-MoS_2) layers, an integrate-and-fire artificial neuron is realized as shown in Figure 5. The developed v-MoS_2/graphene TSM artificial neuron can operate over a wide range of temperature and can potentially be scaled down to nanometer scale cross bar structures. The key characteristics of a biological neuron including an all or nothing spiking, a threshold driven spiking, a post firing refractory period and an input strength modulated frequency response can be emulated by the developed artificial neuron**.** This platform provides an attractive prospect for neuromorphic circuits, which can be seamlessly integrated with existing fabrication technologies enabling large scale realization of such devices.

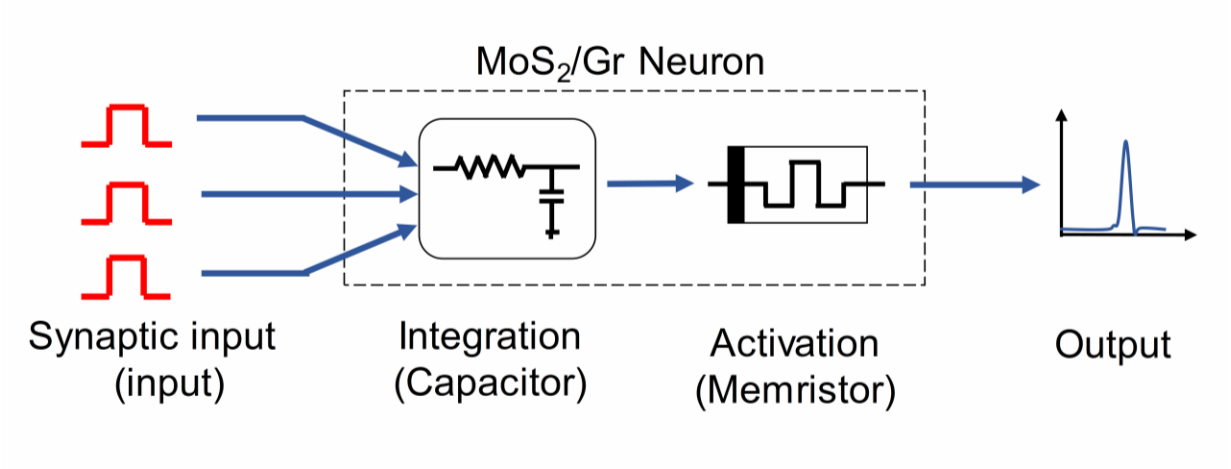

Figure 5. Conceptual representation of the v-MoS_2/Graphene memristor-based artificial neuron.

1.5 Layout of the thesis

This thesis has been organized into five chapters. Chapter two describes the fabrication and characteristics of IMT devices using 1T-TaS_2. The MoS_2/Graphene threshold switching memristor is explained in detail in chapter three. The design and output characteristics of the artificial neuron is described in chapter four followed by chapter five which is the conclusion.

CHAPTER 2 : INSULATOR TO METAL TRANSITION IN 1T-TAS2

2.1 Introduction to 1T-TaS_2

It has been observed that TMDs such as $TaSe_2$, TaS_2, $TiSe_2$, $NbSe_2$ etc. show a phase transition property from a conducting state to a non-conducting state. One of the most interesting materials is 1T-TaS_2 as it shows a temperature dependent as well as electric field dependent Phase transition[22, 23]. Various materials such as VO_2, NbO_2 etc. also show a phase transition and the underlying phenomenon have been widely studied. The origin of these phase transition in 1T-TaS_2 is attributed to the Charge Density Wave (CDW) states switching which arises due to the lattice structure of the material. Various temperature dependent phase transition studies have been done on 1T-TaS_2 to understand the phase transition phenomenon. As the temperature is decreased, clusters of David stars are formed due to the lattice distortion of Ta as shown in Figure 6[22]. With decreasing temperature, the lattice distortion of Ta atoms causes the formation of clusters of David stars where 12 Ta atoms are inclined in moving towards one center Ta atom. Consequently, only one free electron is available in the David star thereby increasing the resistance. It has been studied and reported that 1T-TaS_2 undergoes two PTs during the cooling down process: an incommensurate charge density wave (ICCDW) below 550 K to a nearly-commensurate charge density wave (NCCDW) around 350 K, and then a NCCDW to a commensurate charge density wave (CCDW) around 180 K[22]. 1T-TaS_2 shows an electric field driven charge density wave (CDW) phase transitions (PTs) from the insulating phase referred to as the Commensurate CDW (CCDW) phase to the low resistivity incommensurate CDW phase (ICCDW) with a Nearly Commensurate CDW (NCCDW) phase existing between these two states in which the resistivity is not as high as in the CCDW phase. ICCDW phase has

the lattice completely filled with David stars and in the CCDW phase the crystal has no David star in it with the NCCDW phase being partially filled with David Stars in the crystals exists between CCDW and ICCDW. When thin 1T-TaS_2 flakes i.e. when thickness is less than 24 nm, transition from the NCCDW state to the CCDW state is absent when cooling down the sample[22]. It has been reported that at temperature below 350 K, 1T-TaS_2 undergoes a transition from incommensurate charge density wave (ICCDW) to a nearly-commensurate charge density wave (NCCDW)[22]. In this report, we have studied the dependence of the phase transition on the electric field with different dielectrics.

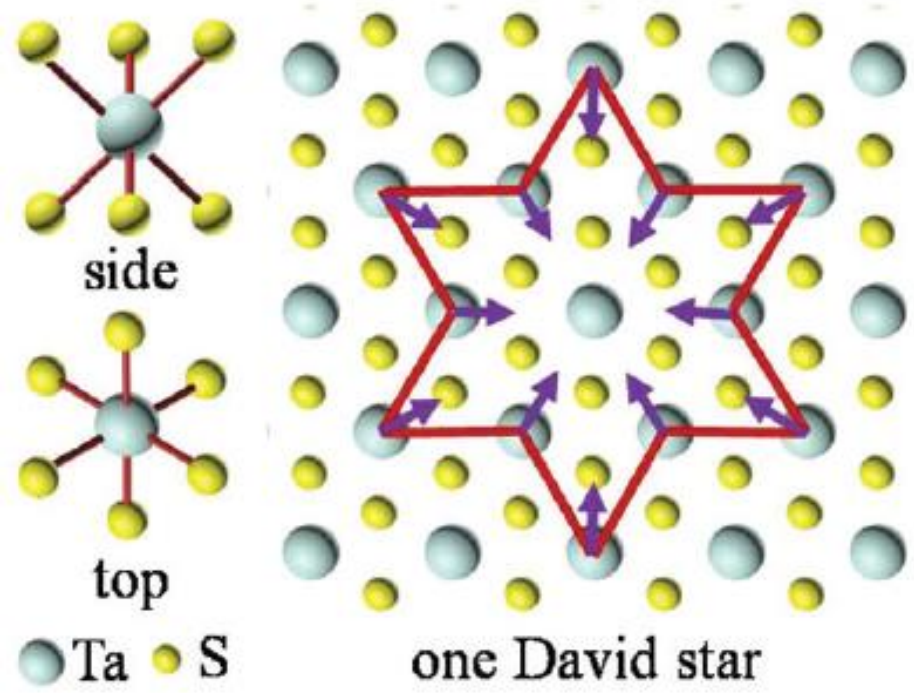

Figure 6. Schematic representation of 1T-TaS_2 structure showing the David star[22]

2.1.1 Material characterization

The 1T-TaS_2 flakes are obtained by mechanical exfoliation. Figure 7 shows an exfoliated 1T-TaS_2 flakes and Figure 8 shows the AFM height image of the exfoliated flake. The thickness of the flake was found to be ~11 nm. The AFM topography was acquired on an Anasys NanoIR2 system in tapping mode using Anasys tapping mode AFM probes (Model No. PR-EX-T125-10). Figure 9 shows the Raman Spectra obtained from the exfoliated flake which yielded three peaks at 100 cm^{-1}, 243 cm^{-1} and 306 cm^{-1} in the NCCDW state at room temperature which is in accordance of the literature.[24]

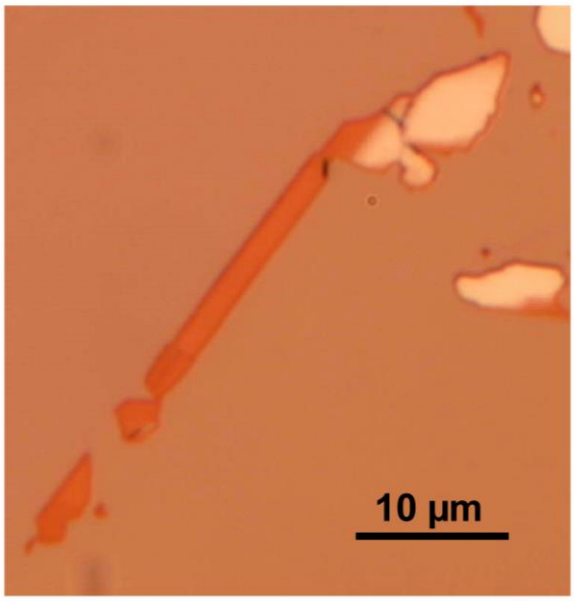

Figure 7. Optical image of an exfoliated 1T-TaS_2 flake

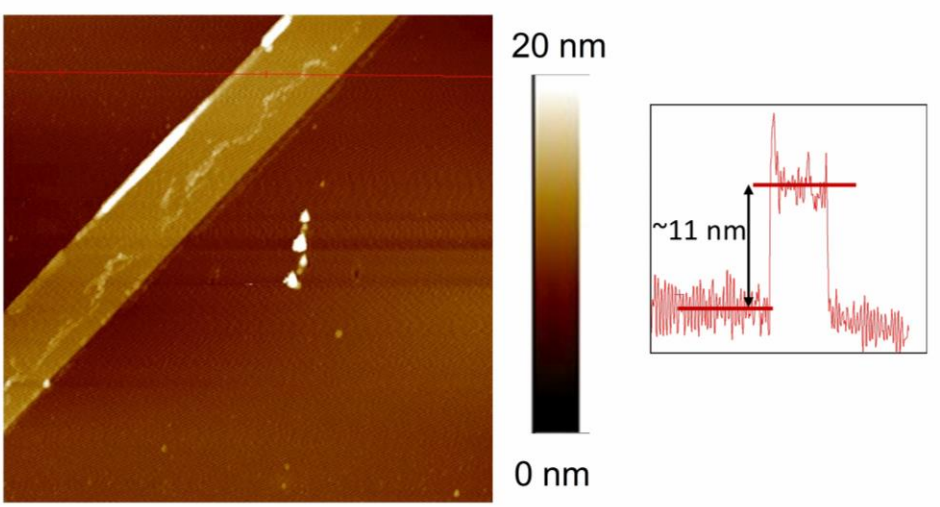

Figure 8. AFM height image of an exfoliated 1T-TaS_2 flake showing the thickness of the flake to be ~11 nm.

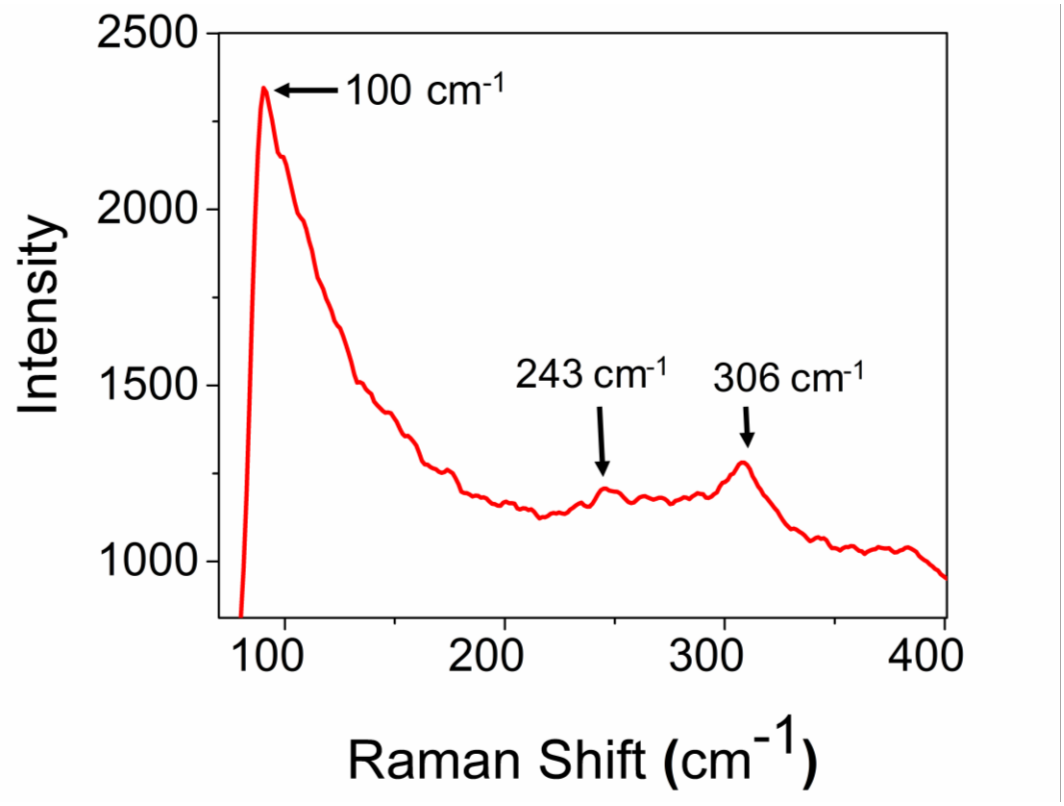

Figure 9. Raman spectrum of the exfoliated 1T-TaS_2.

2.1.2 Device Fabrication

The device schematic is shown in Figure 10. It is a two-terminal device with mechanically exfoliated 1T-TaS_2 flakes being used as the channel material. The optical image of the device is shown in Figure 11. 1T-TaS2 flakes were obtained by mechanical exfoliation on a commercial Si/SiO_2 (260 nm) substrate. Contacts to the 1T-TaS_2 flakes were patterned using Electron Beam Lithography and Nickel was deposited using Electron Beam Evaporation.

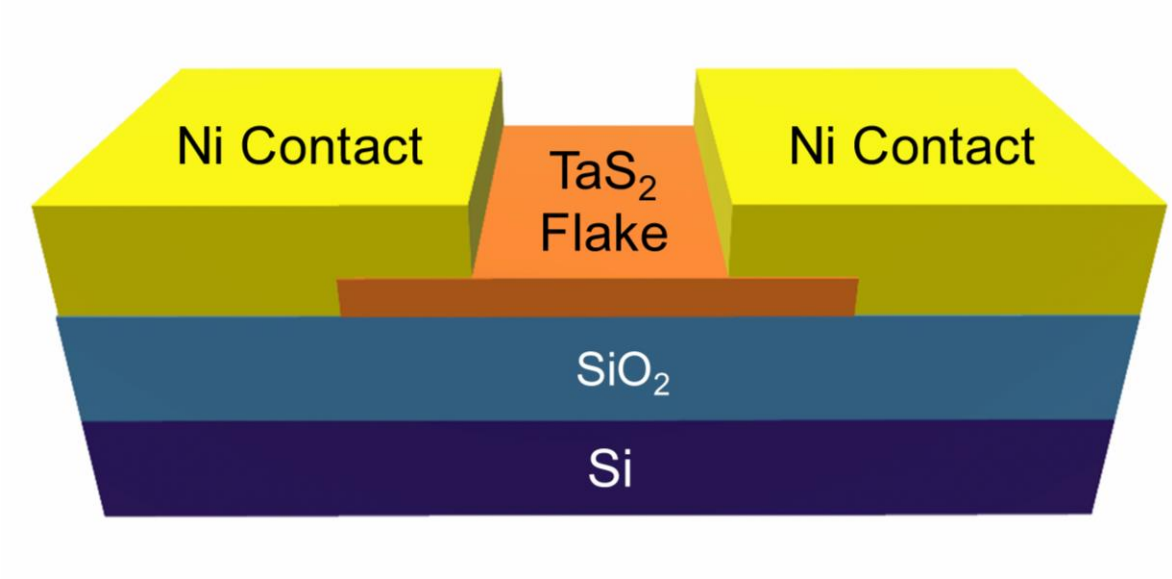

Figure 10. Schematic of a 1T-TaS_2 device.

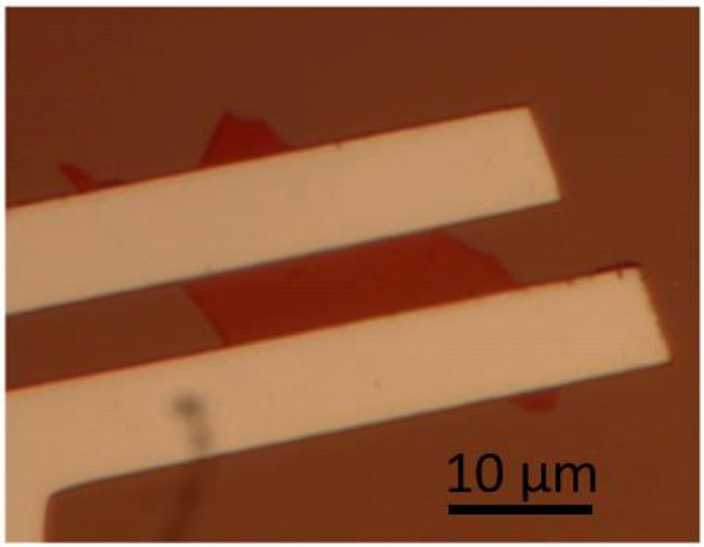

Figure 11 Optical image of the device

2.1.2.1 E-Beam Lithography

The sample containing the exfoliated 1T-TaS_2 flakes on it is spin coated with the E-Beam resist. The resist used for this step is MicroChem 950 PMMA C4 and the sample is rotated at 500 rpm for 30 secs followed by 4000 rpm for 30 sec. The sample is then soft baked at 130°C for 3 mins. The e-beam lithography is completed using a Zeiss Ultra 55 scanning electron microscope (SEM) integrated with Nanometer Pattern Generation System (NPGS) and the mask design files are created using DesignCAD. The smaller patterns (contact fingers) are written at a current ~100nA with a dose of 350 µC/cm^2 while the larger patterns (contact pads) are written with a current of ~1.4nA and a similar dose of 350 µC/cm^2. The sample is then immersed in a mixture of MIBK: IPA in the ratio of 1:3 for 45 seconds followed by an IPA bath for 1 min.

2.1.2.2 E-Beam Evaporation

Next the substrate is loaded onto the evaporator and 50nm Nickel is deposited by e-beam evaporation. The metal needs to be lifted off and hence the sample is placed in an acetone bath at 60°C for 20mins. This removes the resist as well as the metal from all over the sample except the two patterned contacts.

2.1.3 Electrical Characterization

Figure 12 shows the I-V characteristics of the TaS_2 device with a current compliance of 8mA. Initially the device was in the high resistance CCDW phase. When a voltage higher than the threshold voltage of the device was applied, the device underwent a transition from the CCDW phase to the low resistance ICCDW phase. This electrically driven insulator to metal transition (IMT) usually occurred at a critical field which was 5.46 kV/cm in this case. The voltage at which the device switches from the high resistance state (HRS) to the low resistance state (LRS) is referred to as V_1 and that from the low resistance state to the high resistance state is V_2

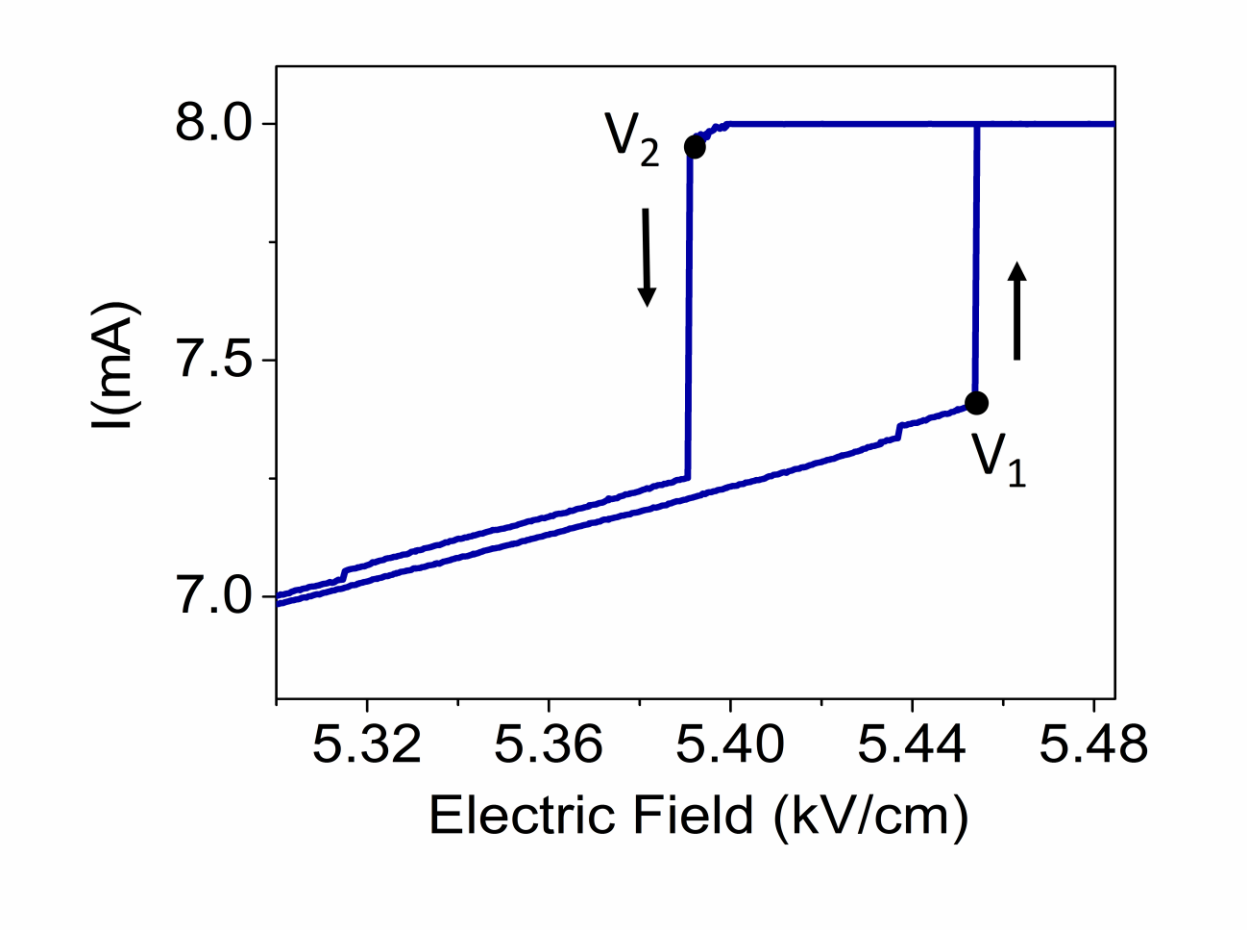

Figure 12. I-V characteristic of the 1T-TaS_2 device showing a clear Phase transition.

To gain more insight into the IMT transitions, the DC characteristics of the device were studied for over 200 cycles and it was observed that the device retained the abrupt phase transition over this period as seen in Figure 13. The obtained V_1 and V_2 were plotted over the same period as seen in Figure 14. It can be inferred that the critical voltage for the transition for the IMT (both V_1 and V_2) doesn't follow any particular trend over the cycling period and shows a stochastic behavior. Figure 15 shows the cumulative distribution function of the 1T-TaS2 device undergoing a IMT transition.

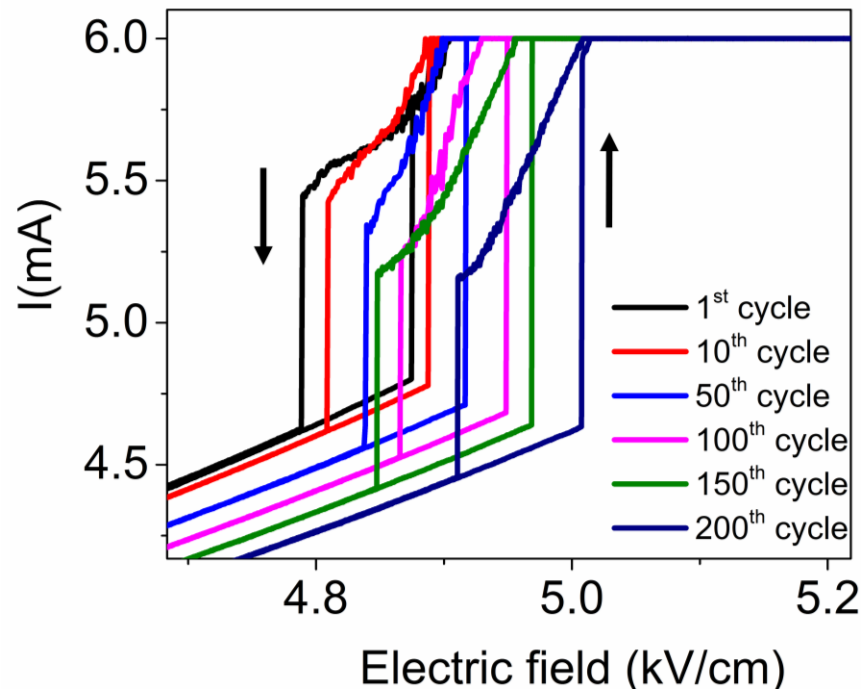

Figure 13. I-V characteristics of 1T-TaS_2 over 200 cycles

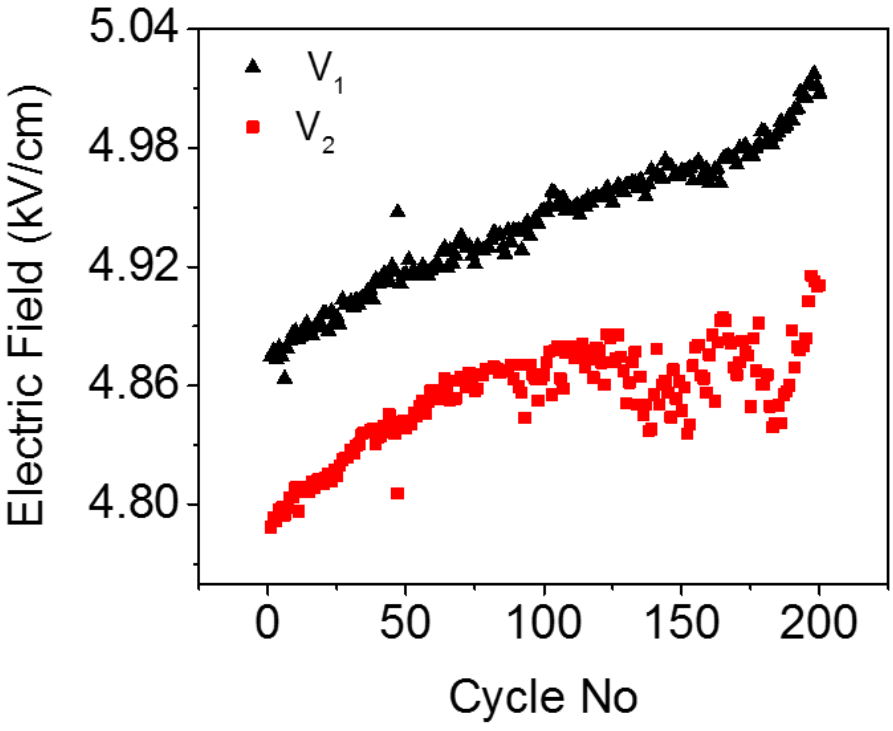

Figure 14. Variation of V_1 and V_2 over the measured 200 cycles.

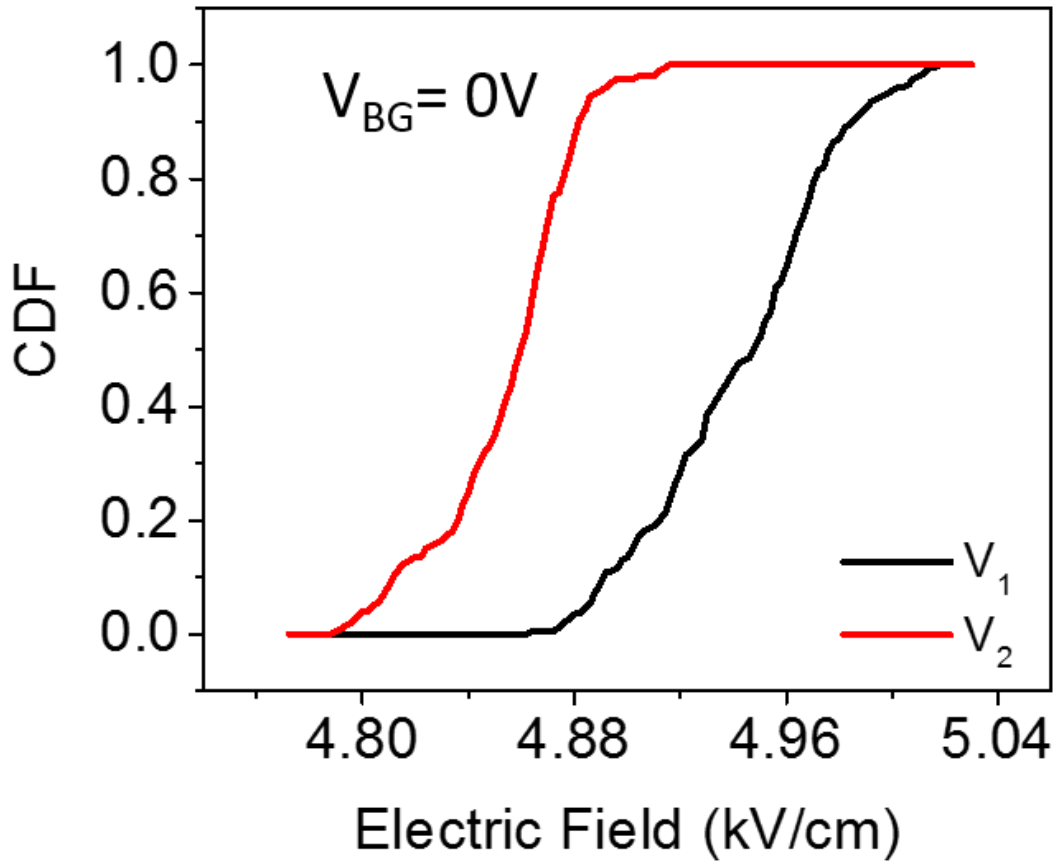

Figure 15. Cumulative distribution function of V_1 and V_2.

Realization of an artificial neuron using 1T-TaS_2 did not materialize as the difference between the resistance in the NCCDW and CCDW states is not sufficient to realize the spiking behavior. Also, it is noticed from the experiments that the 1T-TaS_2 gets damaged (is burnt) on the application of input pulses. This might be due intrinsic material characteristics of 1T-TaS_2 which requires further studies.

2.1.4 Gate Dependence Study

There have been reports of a gate tunable phase transition in 1T-TaS_2 using solid electrolyte.[25] In this section, we will study the effect of an applied gate voltage on the critical field for IMT in 1T-TaS_2 using a 260nm SiO2 (with dielectric constant, κ ~3.9) as the backgate. An input voltage of -100V applied to the gate and the device is cycled for 125 times. It is observed from the experiment that the device retains the stochastic IMT characteristics all throughout the period of 125 cycles as seen in Figure 16. It is however very interesting to note that the there is a distinct change in the critical field required for IMT in 1T-TaS_2 on the application of a gate voltage. Figure 17 shows the cumulative distribution function for the IMT in 1T-TaS_2 without any gate voltage and with a gate voltage of -100V. It clearly shows that with an applied gate voltage -100V on 260nm SiO_2, the critical voltage can be varied to the order of ~1kV/cm. Using a 260nm gate dielectric is not viable practical scaling purposes. Hence, we propose a novel structure using 1T-TaS_2 and Ta_2O_5 as the dielectric to further study the gate modulated IMT in 1T-TaS_2.

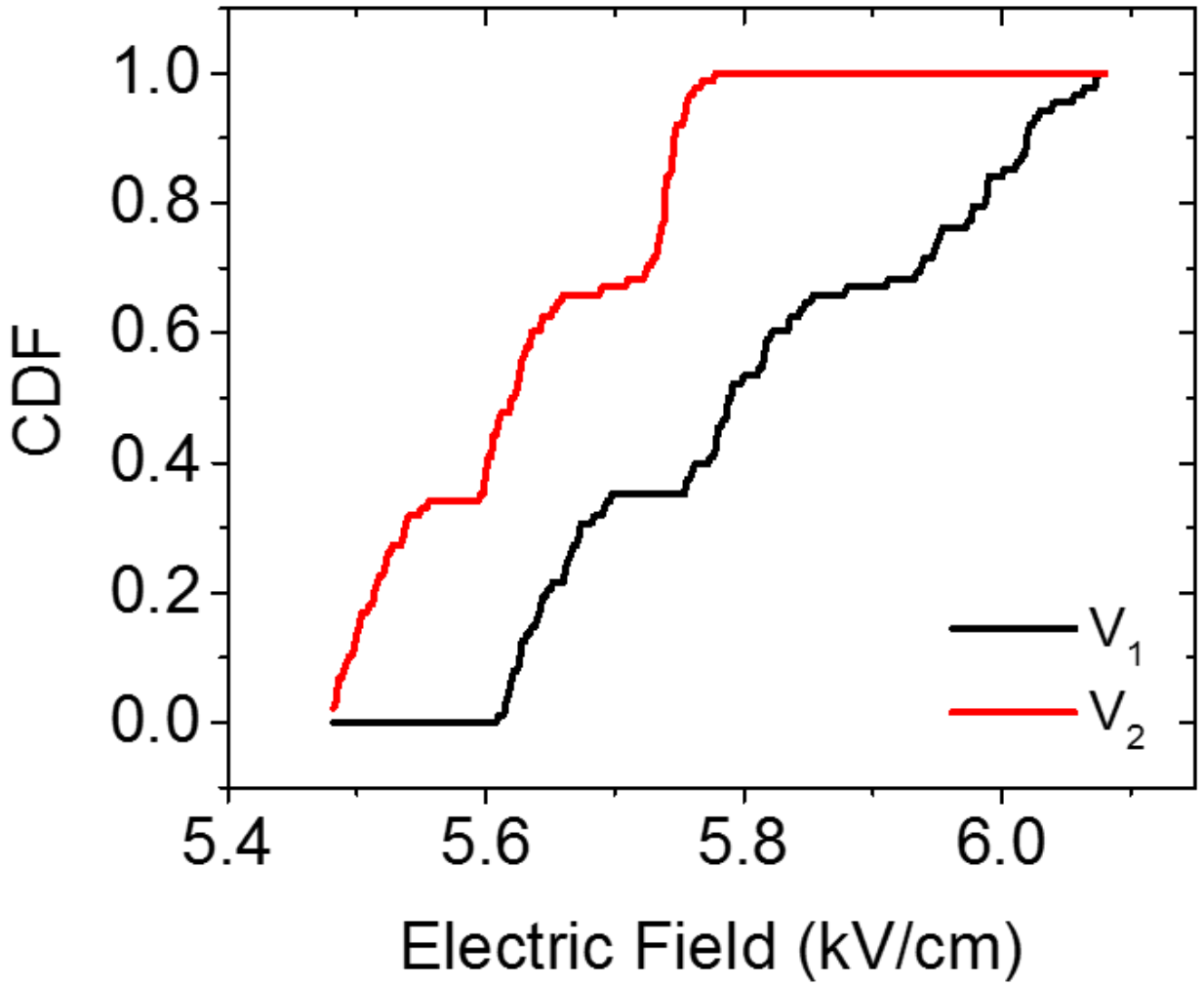

Figure 16. Cumulative distribution function of V_1 and V_2 with an applied voltage of 100V on the back-gate

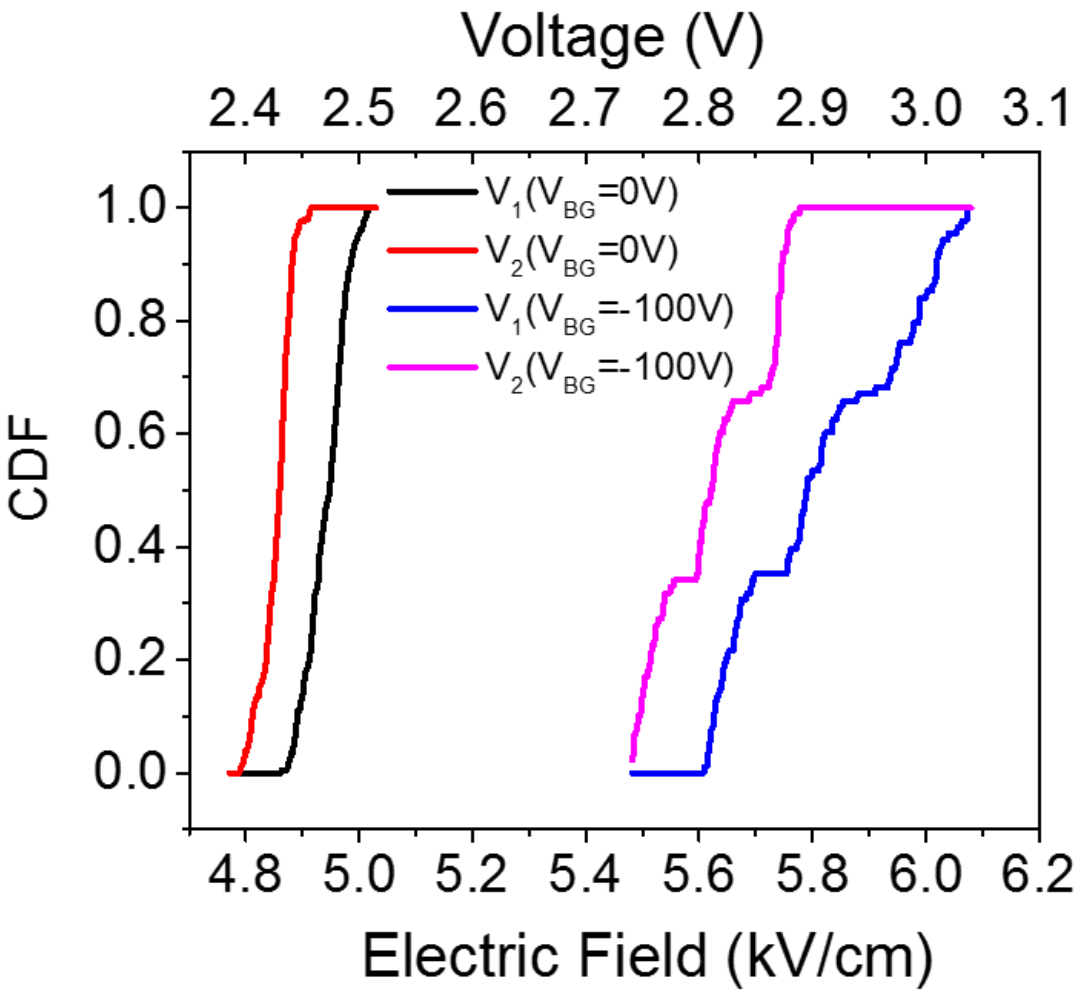

Figure 17. Comparison of the Cumulative distribution function of IMT in 1T-TaS_2 with and without an applied gate voltage.

2.2 TaS_2/Ta_2O_5 Introduction

Recently, there have been reports in which thermally oxidized 2D TaS_2 (Ta_2O_5) has been used a high-κ gate dielectric (with κ ~ 15.5) for MoS_2 field-effect transistors.[26] This report shows huge promise and opens up a plethora of studies for this 1T-TaS_2 material system. Hence,

an integrated system can be derived from 1T-TaS_2 in which the dielectric properties of Ta_2O_5 can be exploited to modulate the IMT of 1T-TaS_2.

2.2.1 TaS_2/Ta_2O_5 Device Fabrication

Figure 18 shows the representative schematic of the device in which a graphene electrode is used as the (bottom) gate of the device and 1T-TaS_2 is used as the conducting channel. The dielectric layer of Ta_2O_5 is sandwiched between the graphene and the 1T-TaS_2. Figure 19 shows the optical image of the fabricated device.

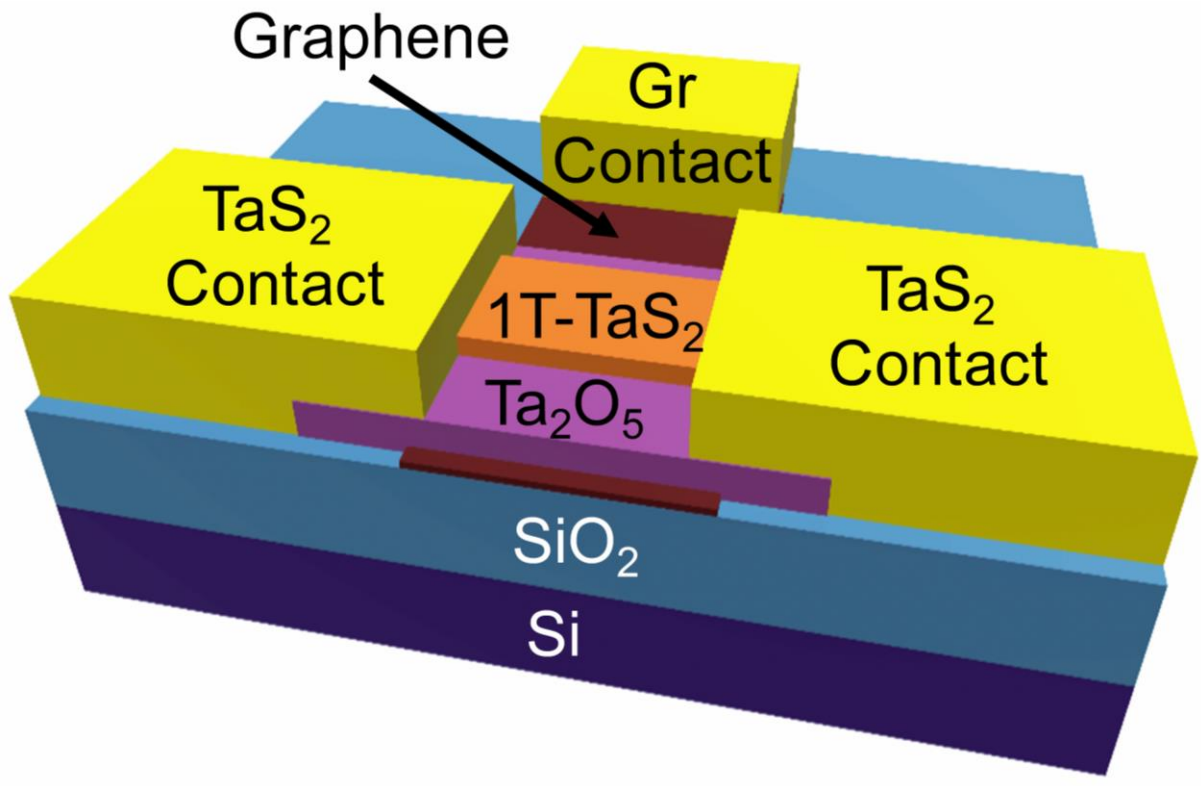

Figure 18. Schematic of a TaS_2/Ta_2O_5 device.

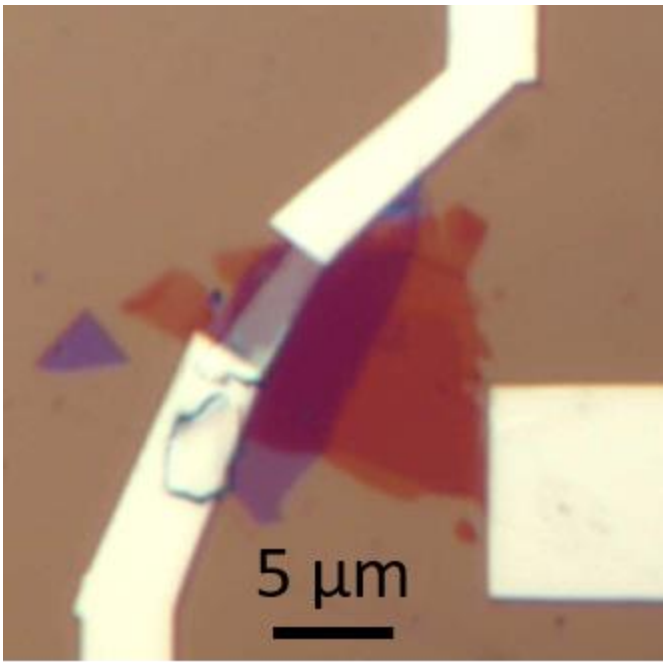

Figure 19 Optical image of the TaS_2/Ta_2O_5 device

Firstly, thin layers (~6-10 layers) of graphene are obtained by mechanical exfoliation on commercial Si/SiO_2 substrate. Then 1T-TaS_2 flakes are exfoliated on the visco elastic stamp and transferred on the exfoliated graphene by dry transfer. The dry transfer setup is an in house developed setup. The flakes are then heated in atmospheric conditions at 300°C for 3 hours. After heating it was observed that the color of the TaS_2 changed to blue signifying that the TaS_2 changed to Ta_2O_5 which is in accordance with the literature.[26] Then another 1T-TaS_2 flake was exfoliated on the visco elastic stamp and transferred on the Ta_2O_5 by dry transfer making the TaS_2/Ta_2O_5 stack. Electrical contacts to the 1T-TaS_2 and the graphene flake were patterned by Electron Beam Lithography and Ni was deposited by Electron Beam Evaporation which are similar to the process described in Section 2.3.1 and 2.3.2.

2.2.2 TaS_2/Ta_2O_5 Gate Modulated IMT Results

Initially the gate voltage applied to the graphene electrode is maintained at the ground level. As the voltage applied to the TaS_2 is increased beyond the critical field, the device undergoes an IMT. Then the gate voltage applied is increased to 1V and it can be clearly seen from Figure 20. that the field at which the IMT occurs by changing the applied gate voltage.

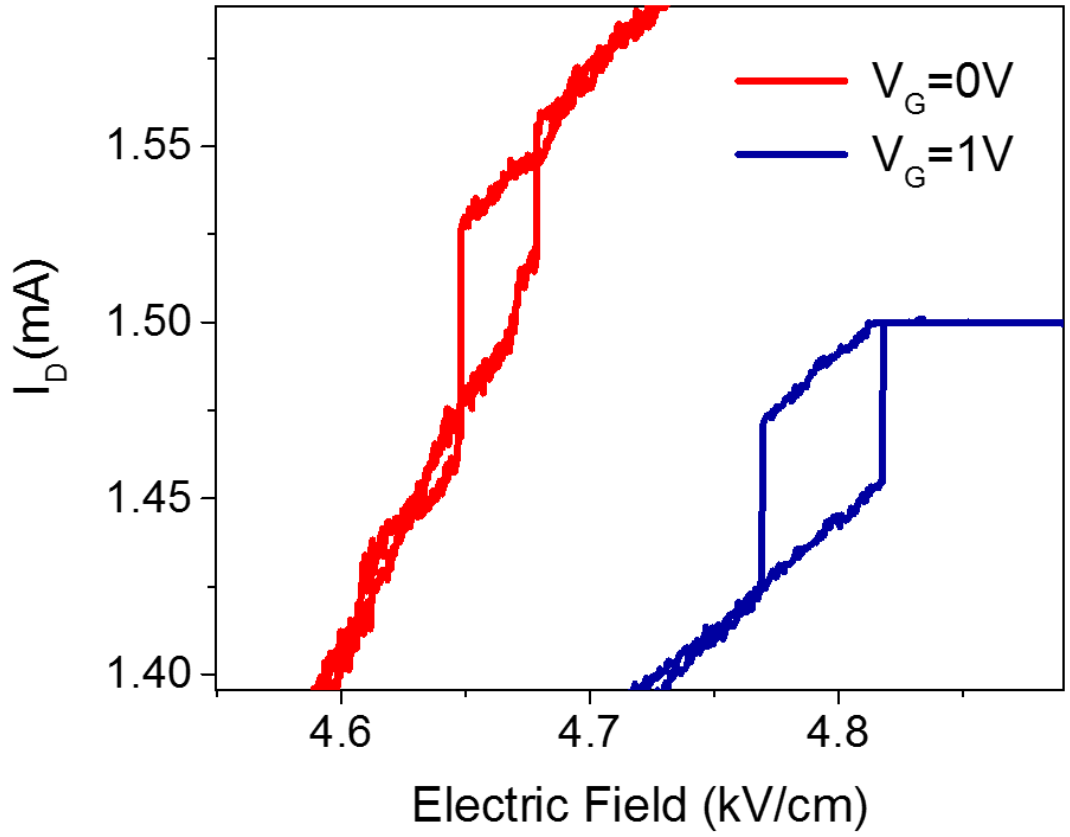

Figure 20. I-V characteristics of the TaS2/Ta2O5 device showing that the phase transition can be modulated by applying a gate voltage of 1 V

CHAPTER 3 : MOS_2/GRAPHENE MEMRISTOR

3.1 Overview

As it is seen in chapter two that the realization of an artificial neuron using 1T-TaS_2 did not bore any fruitful result. Hence, we explore the volatile threshold behavior shown by v-MoS_2/Graphene 2D/2D heterojunction to design an artificial neuron in this chapter.

3.2 Device Schematics and Material Characterization

The device schematic of the v-MoS_2/graphene device is shown in Figure 21. It consists of a CVD-grown monolayer graphene, wet transferred on the Si/SiO_2 substrate[27] followed by patterned growth of v-MoS_2 on graphene. Nickel contacts were deposited on the graphene and on the v-MoS_2. The optical image of the device is shown in Figure 22. Multiple devices have been fabricated on a single chip which enabling large area realization, better scalability, and batch fabrication. A representative picture of the single chip with ~1000 devices is shown in Figure 23.

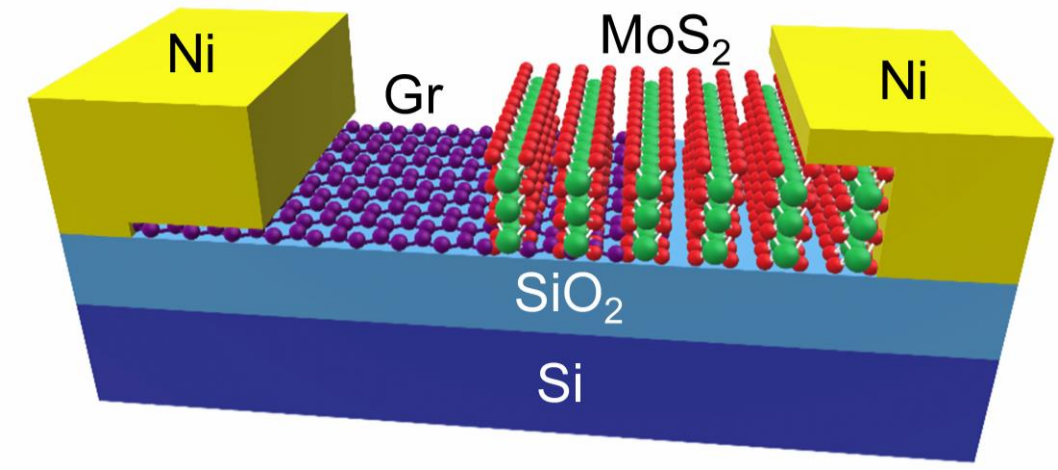

Figure 21. Schematic of a v-MoS_2/Graphene TSM.

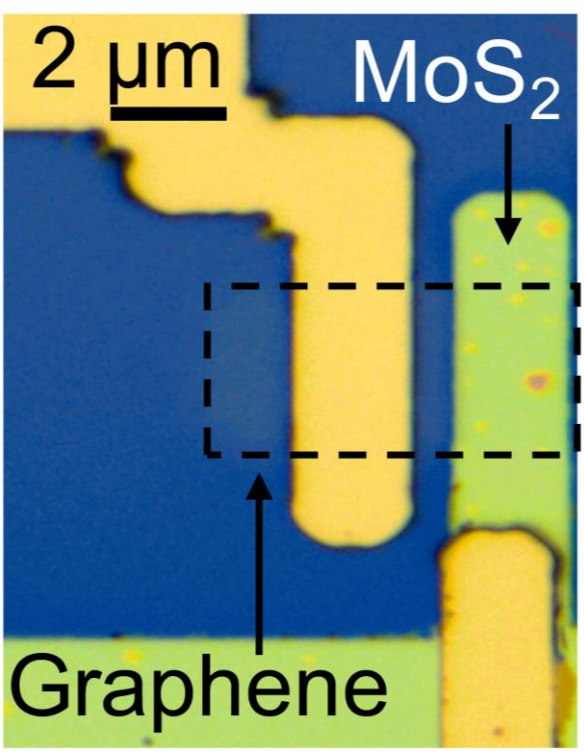

Figure 22. Optical image of the MoS_2/Gr device

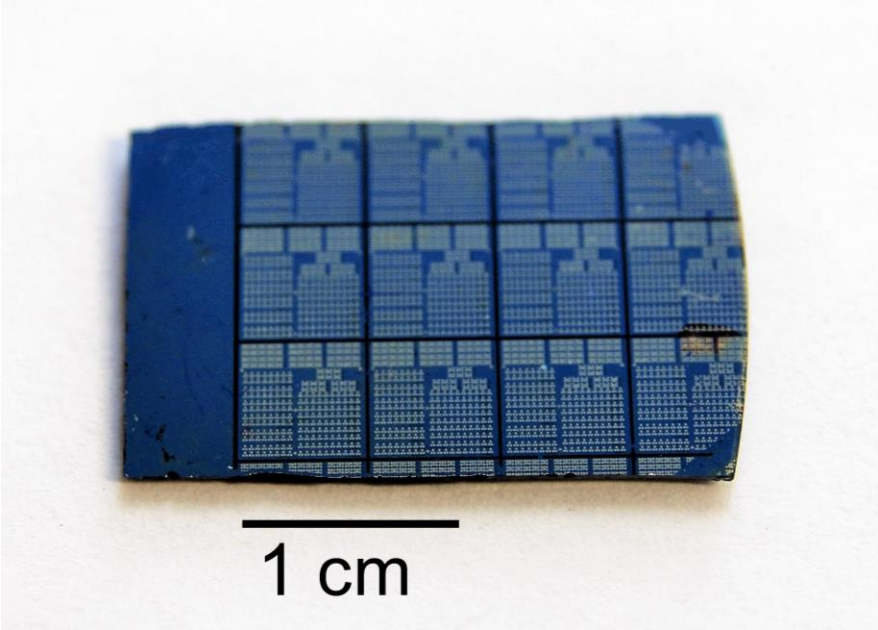

Figure 23. A representative picture of the single chip with ~1000 devices.

The composition of the two layers was confirmed by Raman spectroscopy with excitation wavelength at 532 nm laser in ambient conditions. The spectrum in Figure 24 was obtained on the as grown v-MoS_2 film over graphene in the device. Two bands corresponding to the in-plane E^1_{2g} mode at 383 cm^{-1} and the out-of-plane A_{1g} mode at 411 cm^{-1} were observed. The presence of these two distinct high intensity peaks and the difference of about 28 cm^{-1} between their two positions signifies the presence of good quality multilayer MoS_2.[28]

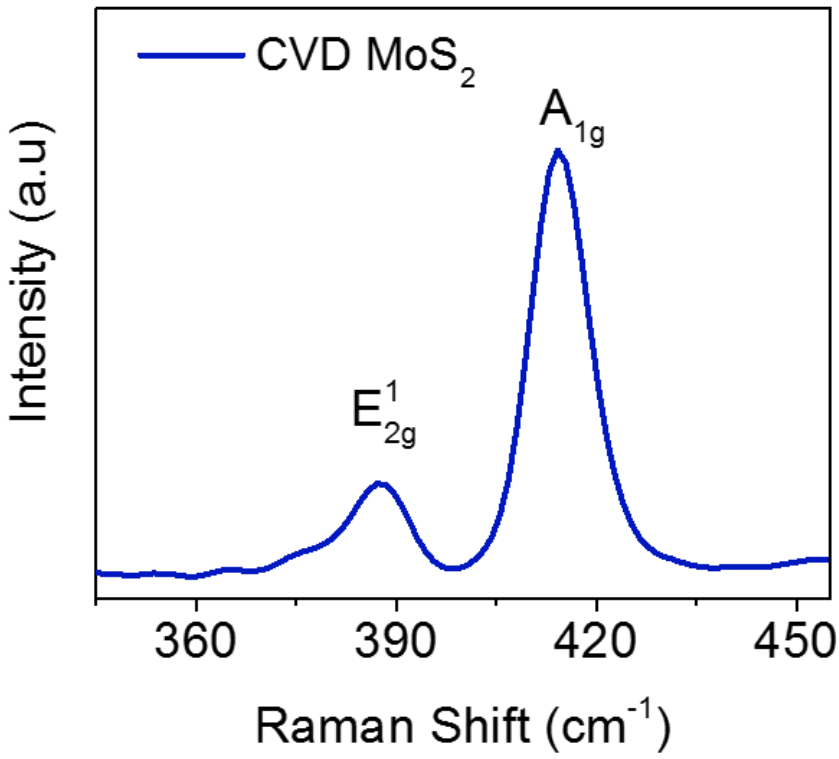

Figure 24. Raman spectrum of the as-grown MoS_2 on graphene.

On pristine graphene, as shown in the inset of Figure 25, the Raman spectrum yielded two major distinct peaks, *viz.* the G band at 1590 cm^{-1}, and the 2D band at 2690 cm^{-1}. The peak

intensity ratio I_{2D}/I_G is about ~2, indicating that the monolayer graphene used for our devices is of good quality.[29] After sulfurization, the spectrum, presented in Figure 26, exhibits three distinct peaks: the D band at 1350 cm^{-1}, the G band at 1590 cm^{-1} and the 2D band at 2690 cm^{-1}. A significant decrease in intensity of the 2D band with respect to the G band is revealed. This reduced value of the peak intensity ratio of the G and 2D peak and the large D band indicate the introduction of defects in the graphene layer during sulfurization[30].

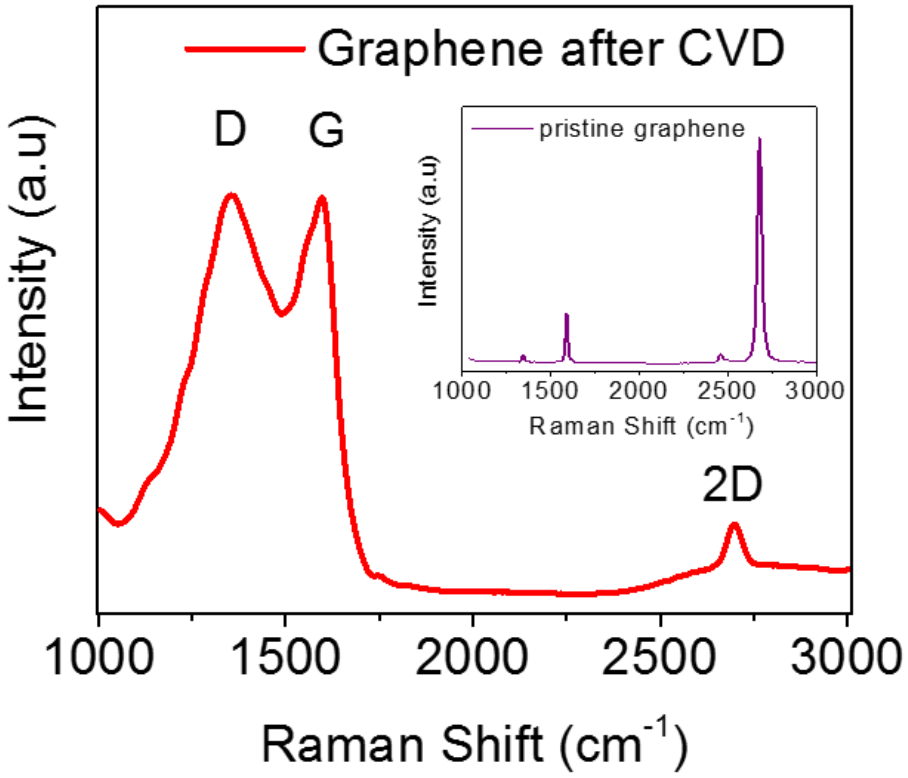

Figure 25. Raman spectrum of the graphene after CVD and the inset shows the Raman spectrum of the pristine graphene.

The detailed analysis of the v-MoS_2/graphene 2D-2D van der Waal's heterojunction was carried out by High Resolution Transmission Electron Microscopy (HRTEM). Figure 26 shows the cross-section HRTEM image of 2D MoS_2 on graphene/Si/SiO_2. It can be clearly observed that MoS_2 grows vertically on the graphene surface with high density of exposed edge planes. The vertical orientation of 2D MoS_2 atomic layers was obtained by the sulfurization of thick Mo films, which essentially minimizes the strain energy arising as a result of volume expansion during Mo to MoS_2 conversion[31]. This eventually leads to the formation of polycrystalline MoS_2 structure with vertically orientated grains perpendicular to the substrate. The thickness of the CVD grown v-MoS_2, as determined by using Atomic force microscopy (AFM) (Figure 27), was 21 nm, which is in agreement with the thickness observed in the cross-section TEM analysis of Figure 26.

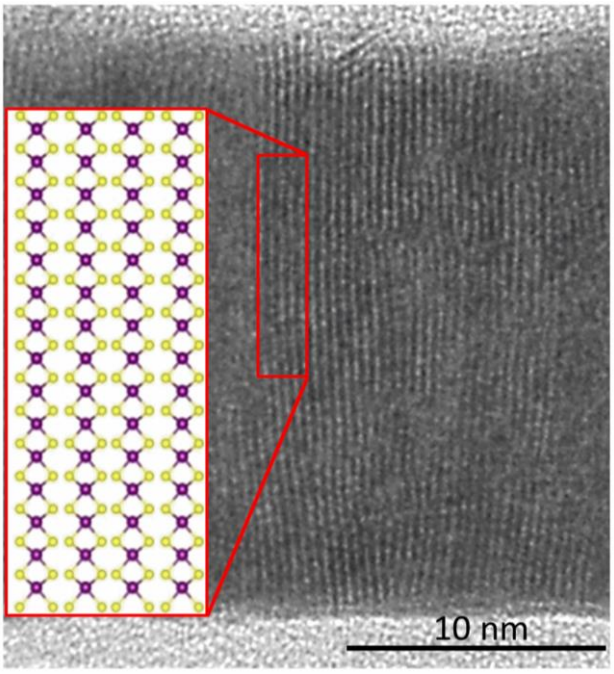

Figure 26. HRTEM image of the cross-section of the v-MoS_2/Graphene interface showing vertical growth of MoS_2.

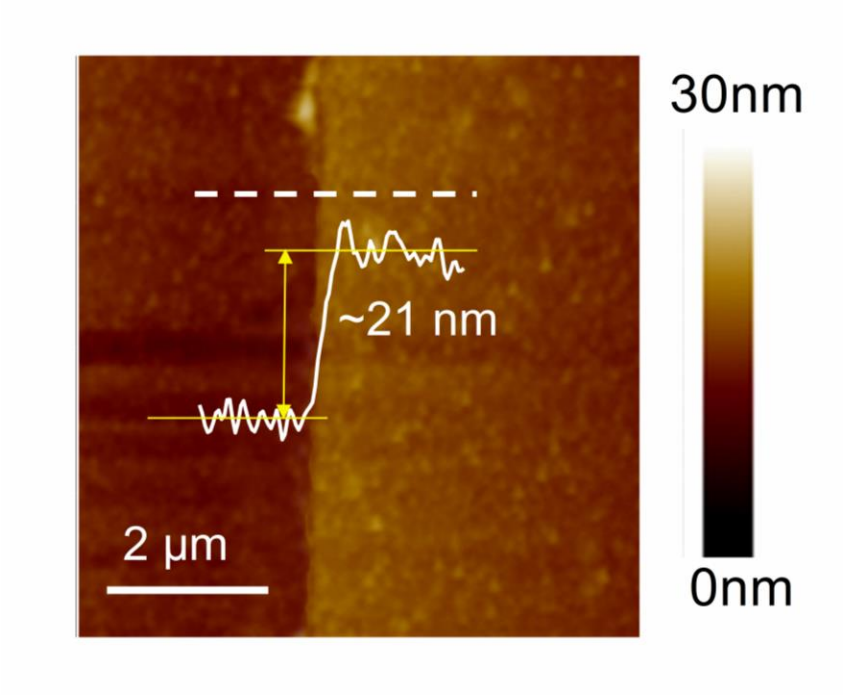

Figure 27. AFM height image of the MoS_2 showing the thickness of the MoS_2 to be ~21 nm.

3.3 Fabrication Steps

3.3.1 Alignment marks patterning

3.3.1.1 Photolithography

A four-level mask designed in house is used for the photolithography. A commercial Si/SiO2 (300 nm SiO2) wafer is cut into ~2 × 2 cm^2 pieces which is then cleaned with acetone and IPA. The chip is coated with a positive photoresist (PR) Microposit S1813. It is then spun at 4500 rpm for 1 min with 3000 rpm/sec acceleration, and then soft bake for 1 min at 115°C. After spin-coating, the sample is loaded to the MicroTec MJB 4 mask aligner for exposure to ultraviolet (UV) light for 9 secs for graphene patterning. The first level mask used for the

alignment marks is shown in Figure 28. Then the sample is placed in a developer (Microposit CD26) to remove the soluble photoresist from the substrates and develop the pattern. It is very crucial to optimize the development time as under-developed patterns will have PR residuals, while over-developed samples can lead to etching issues. Therefore, the development time is optimized carefully for this work and is found that 35 secs is perfect for developing the patterns.

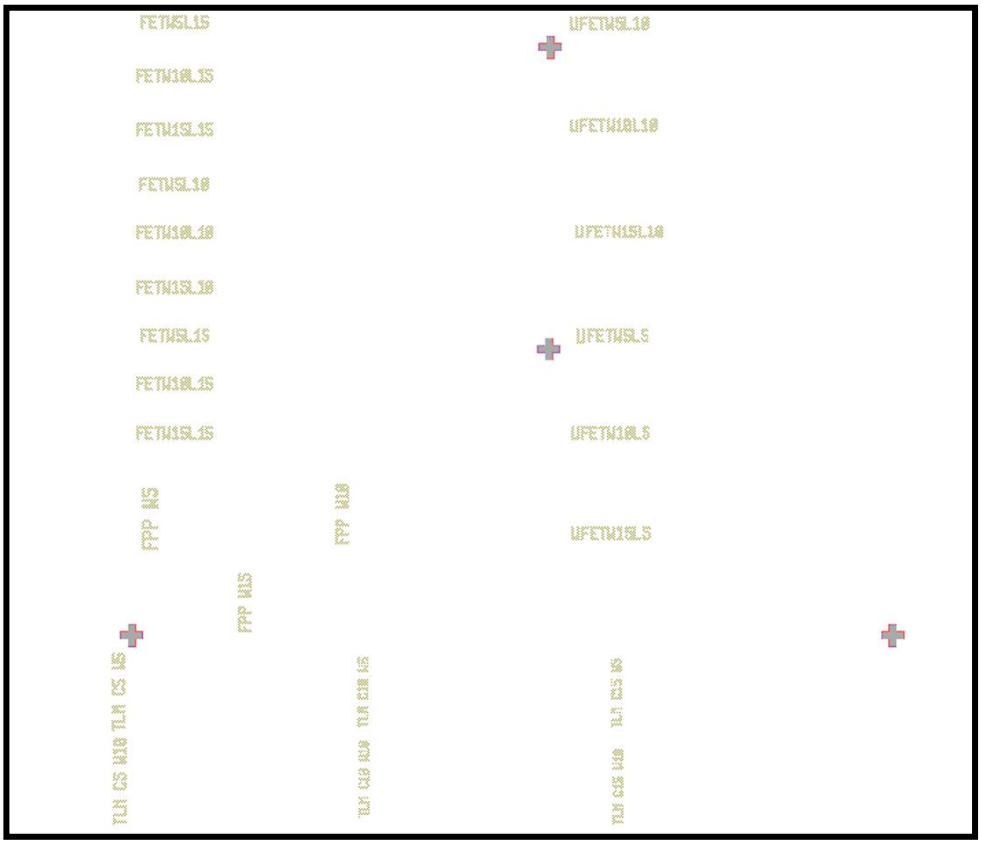

Figure 28. The first level mask used for patterning the alignment marks for fabricating the MoS_2/graphene devices.

3.3.1.2 Metal Deposition

Next the substrate is loaded onto the evaporator (Temescal FC-2000) and 30nm Chrome followed by 30nm Gold is deposited by e-beam evaporation. The sample is placed in an acetone

bath and ultrasonicated for 30 secs for lift off. This removes the resist as well as the metal from all over the sample except the two patterned contacts.

3.3.2 Graphene Transfer

Firstly, PMMA is dissolved in chlorobenzene with a concentration of 46mg/mL and the mixture is allowed to stand still for 4-6 hours so that the chlorobenzene gets completely dissolved. The commercially available graphene/Copper(Cu) stack is spin-coated with PMMA in two steps: first at 3000rpm for 60sec followed by 1000rpm for 60sec. The backside of the graphene is then etched by oxygen plasma using a Plasma Etch PE 50 etcher for 1 min 30 secs with power ~25Watt. The Cu is then etched away in a 0.5 M ammonium persulfate solution overnight. The graphene/PMMA stack is then placed in either deionized (DI) water or IPA before transferring to a Si/SiO2 substrate with alignment marks (described in section 3.3.1) and blow-dried with dry N2. The sample is then heated on a hot plate in air at 220 C for 5 min. This temperature is selected because it is slightly higher than the PMMA glass transition temperature (Tg < 165°C), allowing the PMMA to reflow as it is annealed. After cooling the sample to room temperature, the PMMA is stripped by submerging it in acetone for 2.5 hours at room temperature before device fabrication.

3.3.3 Graphene Patterning

After the graphene is transferred over the substrate, it is then patterned by photolithography (described in section 3.3.1.1). A block from the second level mask showing the etch patterns used for pattering the graphene is shown in Figure 29. The sample is then placed in

the oxygen plasma etcher with a flow of 25 Standard Cubic Centimeters per Minute for etching the patterned graphene for 1 min with power 25 watts.

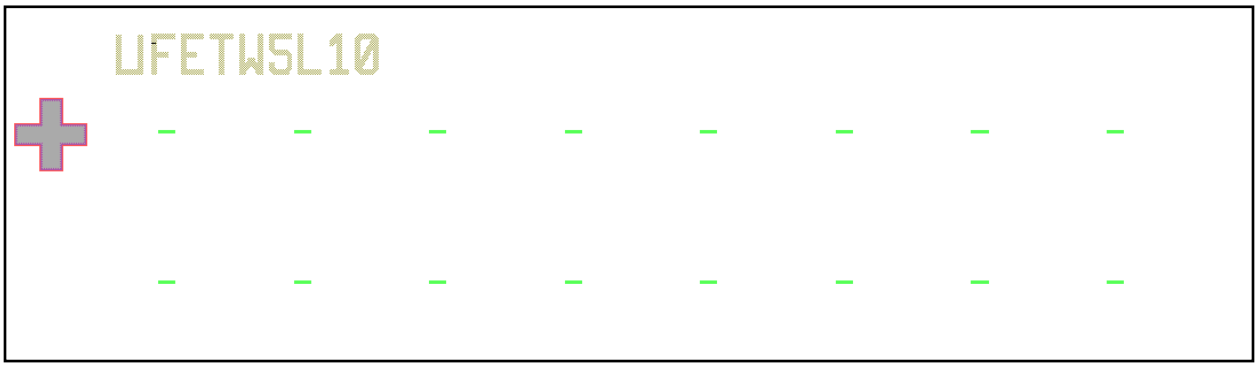

Figure 29. The second level mask used for pattering the graphene

3.3.4 Moly patterning and deposition

The sample was again patterned by photolithography (as described in section 3.3.1.1) for Mo deposition. A block of the second level mask showing the designs for Mo patterning is shown in Figure 30. 10 nm thick Molybdenum (Mo) films were deposited on the patterned substrate using an electron beam (e-beam) evaporation system at a rate of 1Å/sec. The sample is then placed in an acetone bath for 50mins at 60°C which removes the Mo from all over except at the exposed regions. The sample containing the patterned Mo films are subsequently sulfurized to MoS_2 in a low-pressure CVD furnace which will be described in detail in section 3.3.5.

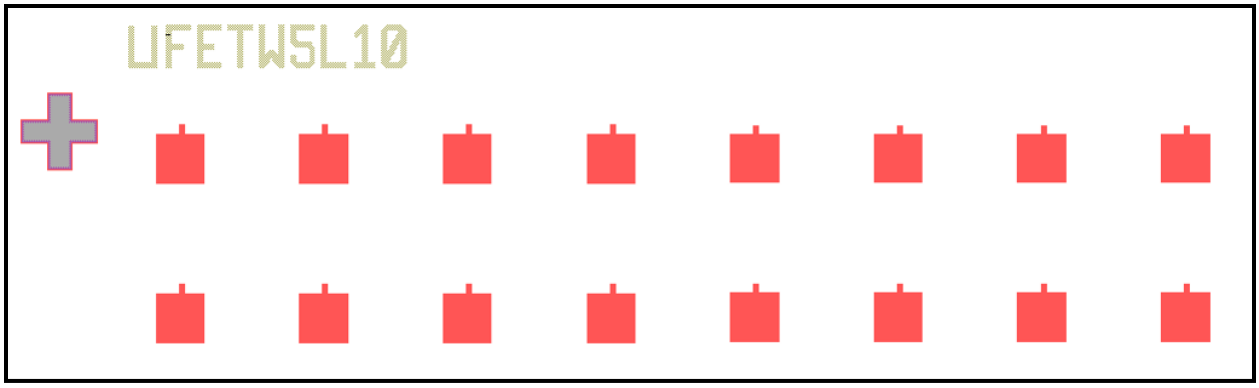

Figure 30. The third level mask used for pattering the Mo

3.3.5 MoS_2 Growth

The patterned Mo film on graphene/Si/SiO_2 substrate are loaded in the center of a quartz tube CVD furnace with a ceramic boat having sulfur powder at the upstream of Mo sample. The furnace was pumped down to a base pressure of ≤1 mTorr and then purged with argon (Ar) gas. The furnace was heated up to a temperature of ~650−700 °C with a constant flow of 100 SCCM (standard cubic centimeters per minute) Ar gas at a pressure of ~100 mTorr. After a 30 min reaction time, the furnace was naturally cooled down and the substrate was taken out of the furnace. The change of color of the substrate from blue to dark green, indicates the sulfurization of Mo on the graphene.

3.3.6 Contacts patterning and metal deposition

Finally, the contacts to MoS_2 and graphene are patterned by two step photolithography and the sample is developed to remove the soluble resist following the same sequence of actions as described in section 3.3.1.1. The third level mask shown in Figure 3.10 is used for patterning the contacts to MoS_2 and the fourth level mask is used for patterning the contacts to graphene as

shown in Figure 31. Then, 50nm Nickel (Ni) is deposited by e-beam evaporation following which the sample is placed in an acetone bath at 60°C for 20mins for metal lift off from all over the sample except the patterned contacts.

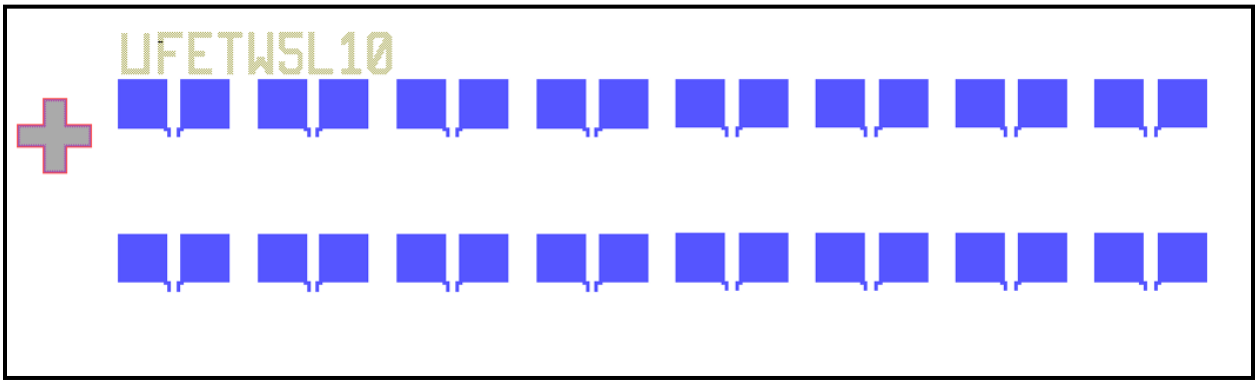

Figure 31. The fourth level mask used for pattering the contacts to graphene

3.4 DC Characteristics

To assess the switching characteristics with respect to the compliance current, the v-MoS_2/graphene TSM was tested at various current compliance of 100 nA, 500 nA, and 1 µA as shown in Figure 32. The I-V characteristics were recorded by sweeping the graphene electrode while keeping the MoS_2 electrode at 0 V. In all the cases, it is observed that the device is in the high resistance state (HRS) until a voltage higher than the threshold voltage is applied. At the onset of the threshold voltage (V_1), the device undergoes an abrupt transition from the high HRS to a low resistance state (LRS). During the reverse sweep, at an applied voltage below V_2, the device again reverts to HRS. It is interesting to note that the device retains the volatile threshold switching behavior for all the applied current compliances.

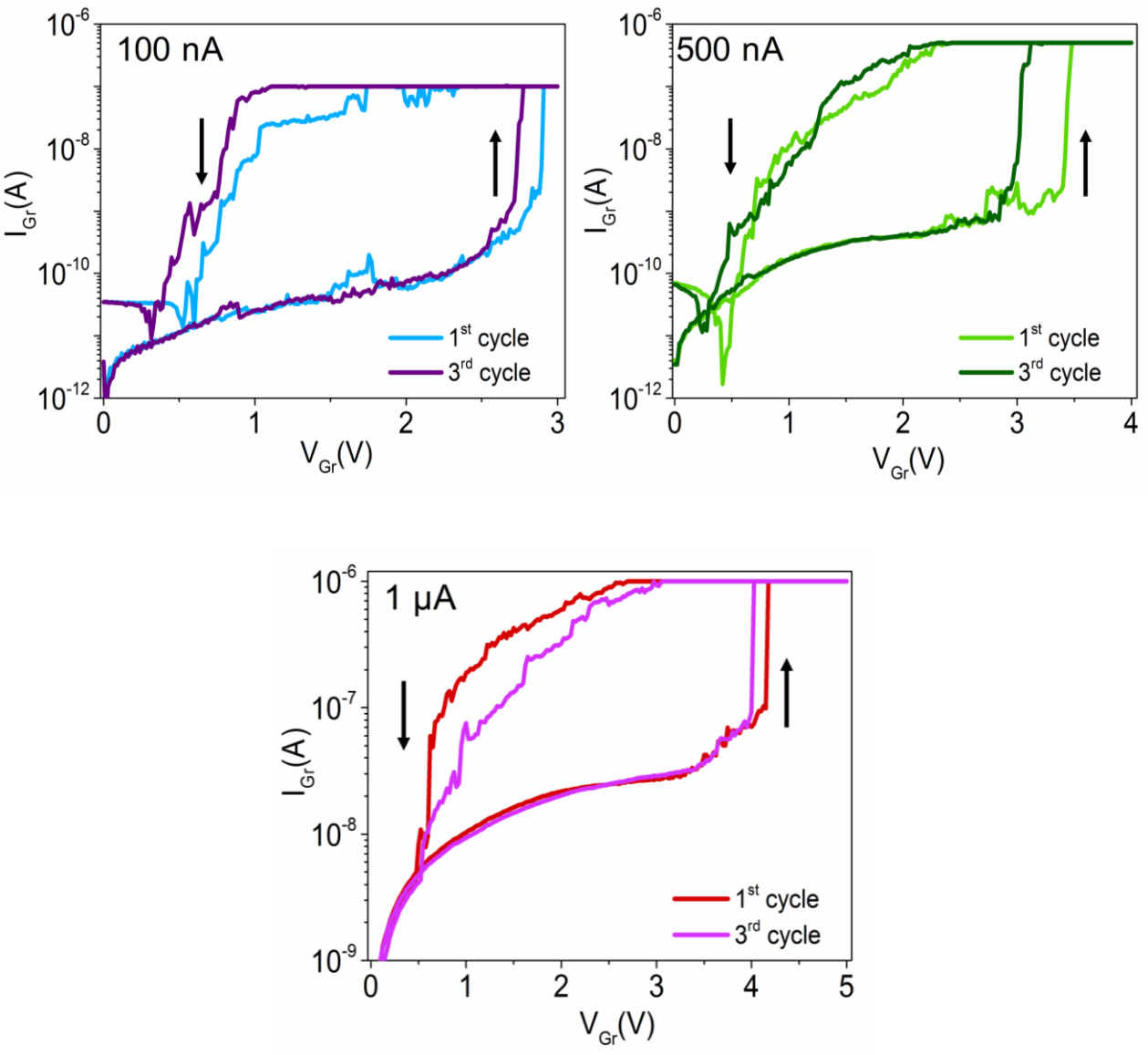

Figure 32. I-V characteristics of the v-MoS_2/Graphene device over multiple cycles showing volatile behavior with a current compliance of (a) 100 nA. (b) 500 nA. (c) 1 µA when the voltage on the Graphene (Gr) electrode is swept keeping the other electrode at 0 V in all cases.

3.5 Switching Mechanism in v-MoS_2/graphene TSM

Recent reports have showed that the switching mechanism in single-layer MoS_2 can be attributed to the grain boundaries (GBs)[20]. The switching behavior of our v-MoS_2/graphene devices can be attributed to the multiple grain boundaries in the polycrystalline films of v-MoS_2. To further comprehend the switching mechanism in the v-MoS_2/graphene devices, the DC measurements were carried out in vacuum. It is interesting to note that in the absence of oxygen, the fabricated devices do not show the volatile switching behavior that was observed in the presence of oxygen as it can be seen from Figure 33. It can be further noted that the switching window disappears and the device doesn't even get reset after that. The vacuum measurements were carried out in a Janis cryo-probe station. Hence, the migration of oxygen ions facilitated by the grain boundaries in the v-MoS_2 is the probable reason the switching mechanism in the realized v-MoS_2/graphene devices.

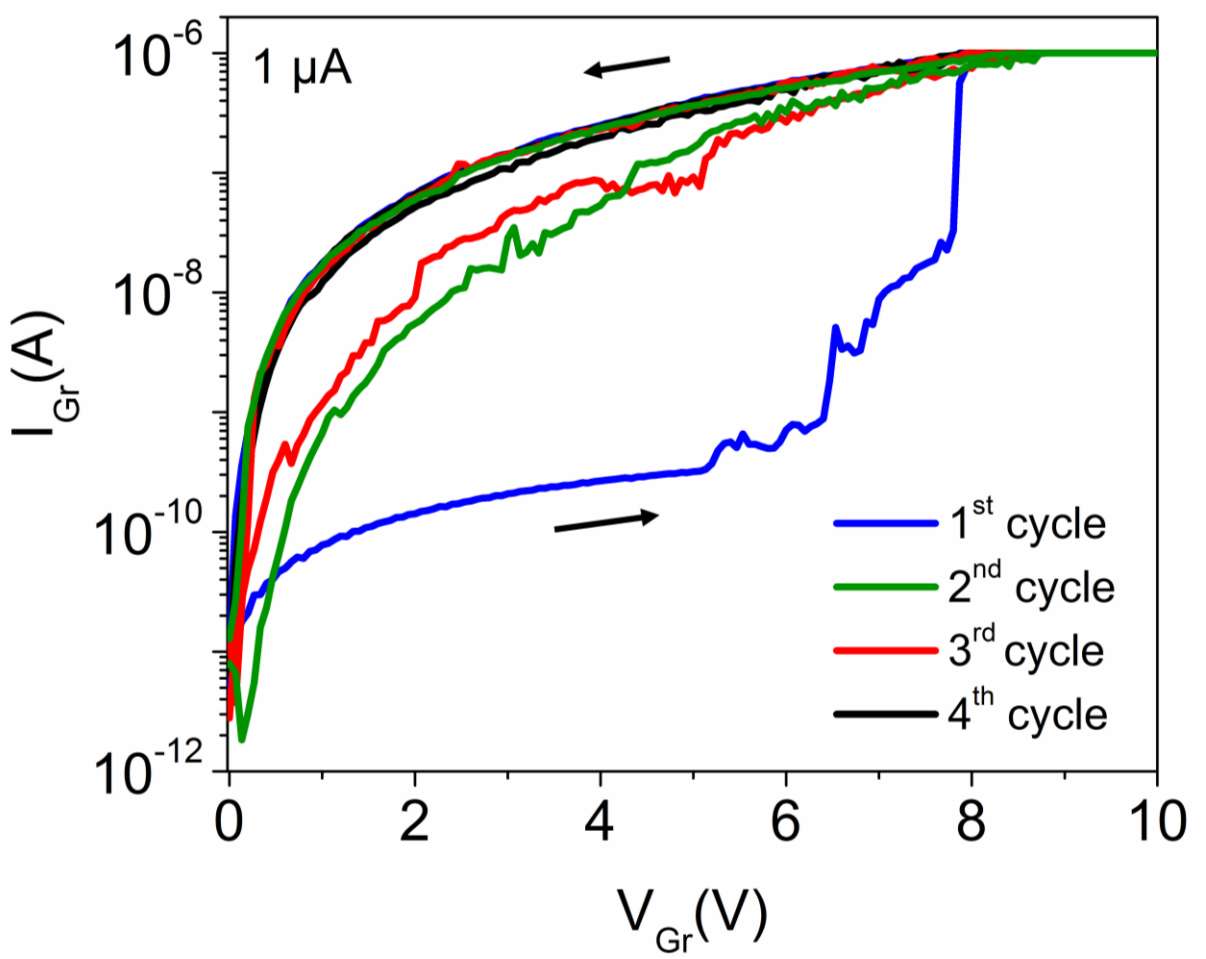

Figure 33. The I-V characteristics of the MoS_2/graphene TSM in vacuum

CHAPTER 4 : REALIZATION OF ARTIFICAL NEURON

4.1 Overview

After confirming the volatile threshold switching behavior of v-MoS_2/graphene device, we now concentrate on the demonstration of an artificial neuron exploiting the volatile switching. A circuit is designed to realize this behavior with the help of the v-MoS_2/graphene TSM. The experimental setup and the results obtained are discussed in the following sections.

4.2 Experimental Setup

The circuit schematic used for realizing the artificial neuron using the v-MoS_2/graphene TSM is shown in Figure 34. The TSM device is connected in parallel with a resistor, R_p=1 MΩ and a capacitor C_0=100 nF which in turn are connected to a synaptic resistance R_0=10 kΩ. The input source is a train of constant amplitude voltage pulses applied to the left node of the circuit with a pulse period of 200 µs and 50% duty cycle. The output current is measured at the rightmost node of the circuit. Figure 35 shows the output current (black line) of the circuit when a series of input pulses of 5 V amplitude and 100 µs width are applied (blue line), which shows charging and discharging of the capacitor with the current increasing and then gets stabilized.

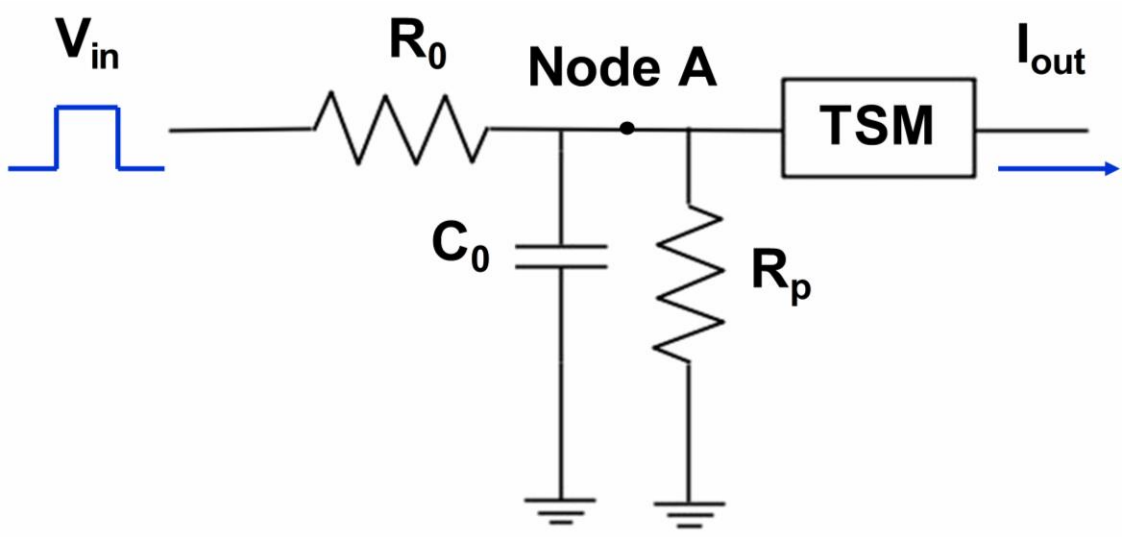

Figure 34. Schematic of the circuit used to realize the artificial neuron.

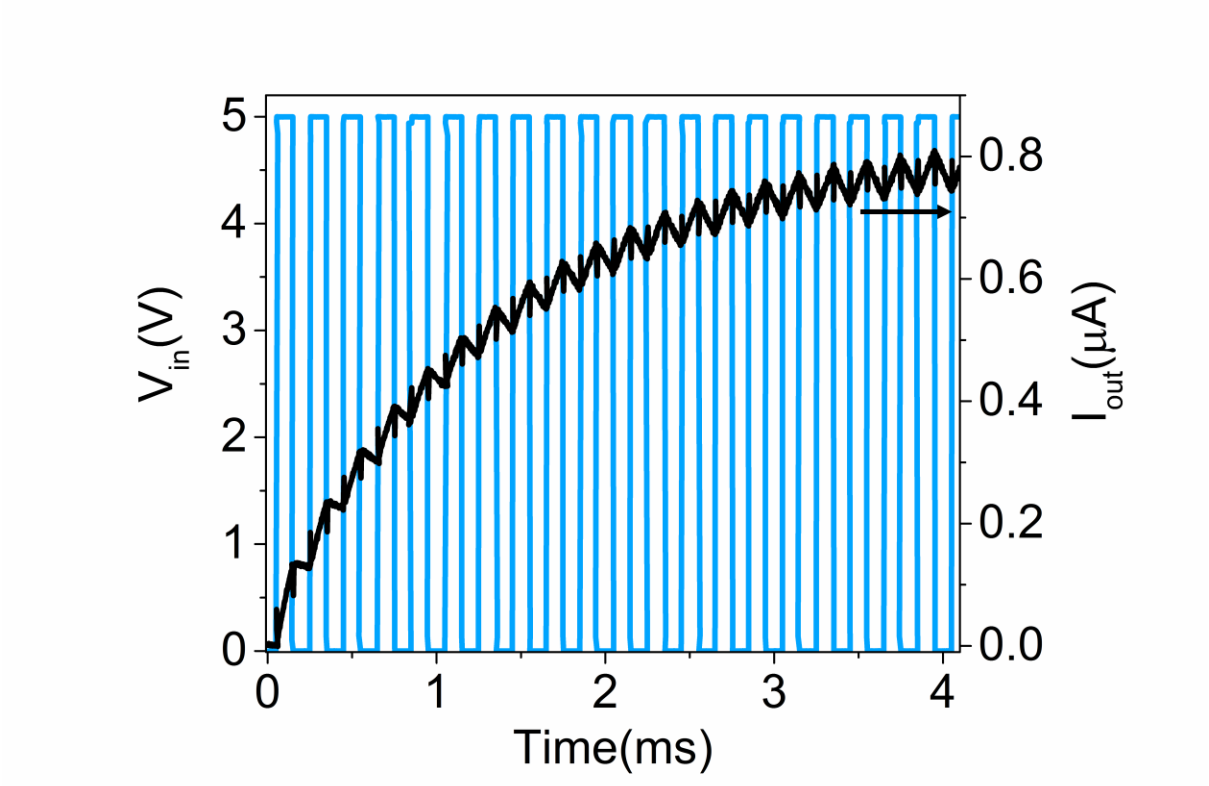

Figure 35. Output current waveform (black line) of the circuit used with 5 V input pulses.

The electrical measurements were carried at room temperature in Micromanipulator 6200 probe station using a Keysight B1500A semiconductor device analyzer along with WGFMUs for pulse I-V measurements. The experimental setup is shown in Figure 36.

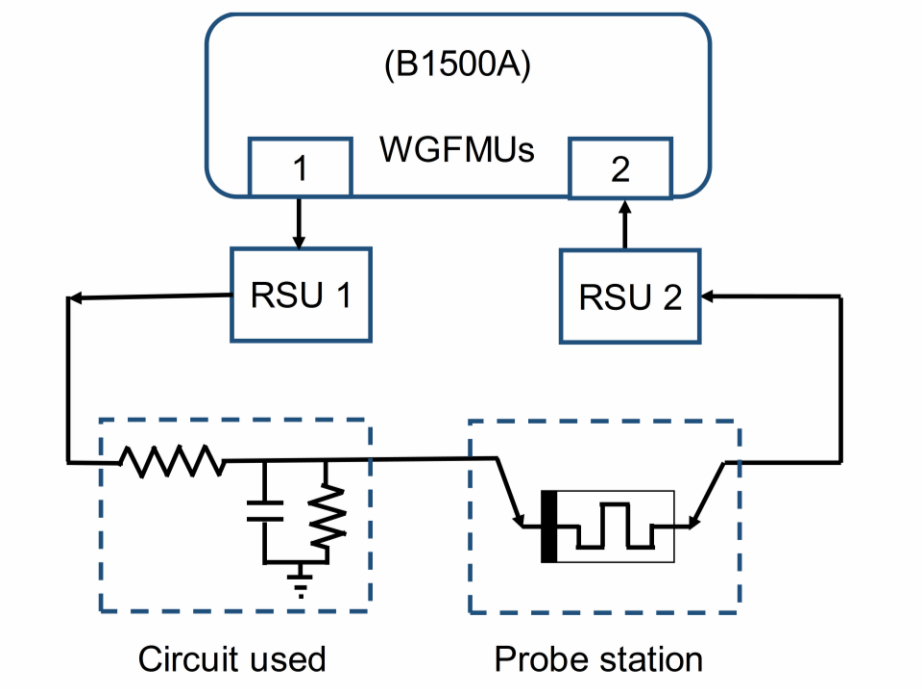

Figure 36. Experimental setup used to obtain the response of the artificial neuron

4.3 Results and Discussion

Initially, the TSM is in its HRS and the device resistance 'R_{HRS}' is high (~10MΩ) compared to R_0. The RC time constant (R_0C) is much less (~ 100x) than that of the device [$(R_p||R_{HRS})C_0$] and the leakage through the device is almost negligible. Therefore, as the input pulses are applied to the circuit, the capacitor (C_0) starts charging. As the charge across the capacitor increases and the voltage across the node A reaches a value beyond the threshold

voltage of the TSM, the device switches from the HRS to the LRS. Since the TSM is now in the LRS state, the capacitor starts discharging through the device and an abrupt increase in the current appears at the rightmost node. Immediately, the capacitor discharges completely and the voltage at the node A starts decreasing, dropping down to the ground level. Once the voltage decreases below 'V_2', the TSM device again reverts to the HRS. Thus, an output current spike is obtained from the artificial neuron. The capacitor starts recharging with commencement of the integration period of the neuron as shown in Figure 37.

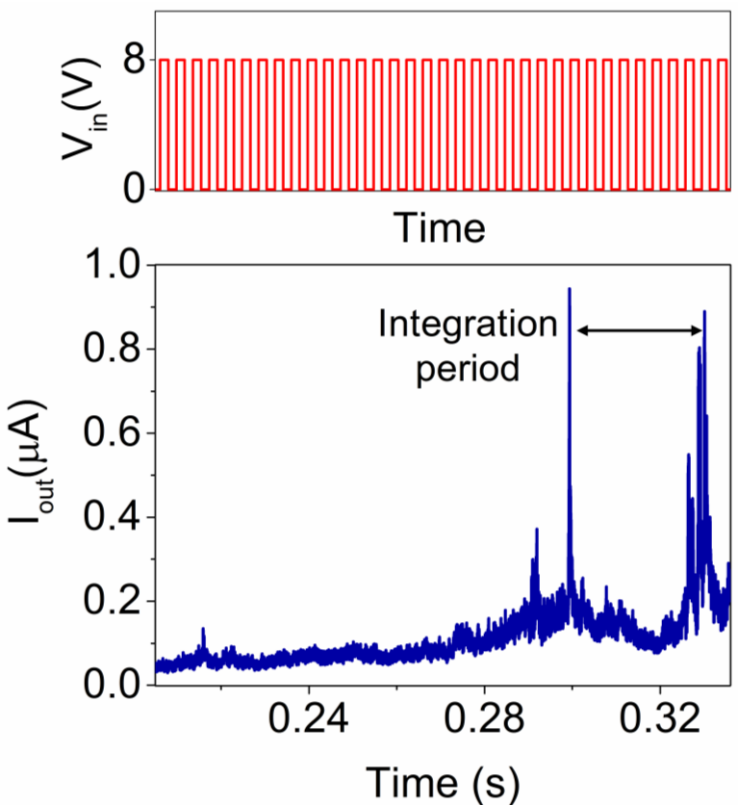

Figure 37. Output spike of the artificial neuron (blue line) showing the integration time along with the representative 8 V input pulses (red line).

During the timeframe when the neuron is firing, the net charge integration across the capacitor is essentially zero. This is because any input voltage pulse applied is being directly drained by the TSM device (it being turned on). This period emulates the post firing refractory period of a biological neuron[1, 4, 17]. Once the refractory period is over, the device reverts to its HRS from the LRS state and the capacitor 'C_0' starts integrating again. The refractory period from the v-MoS_2/graphene TSM is shown in Figure 38.

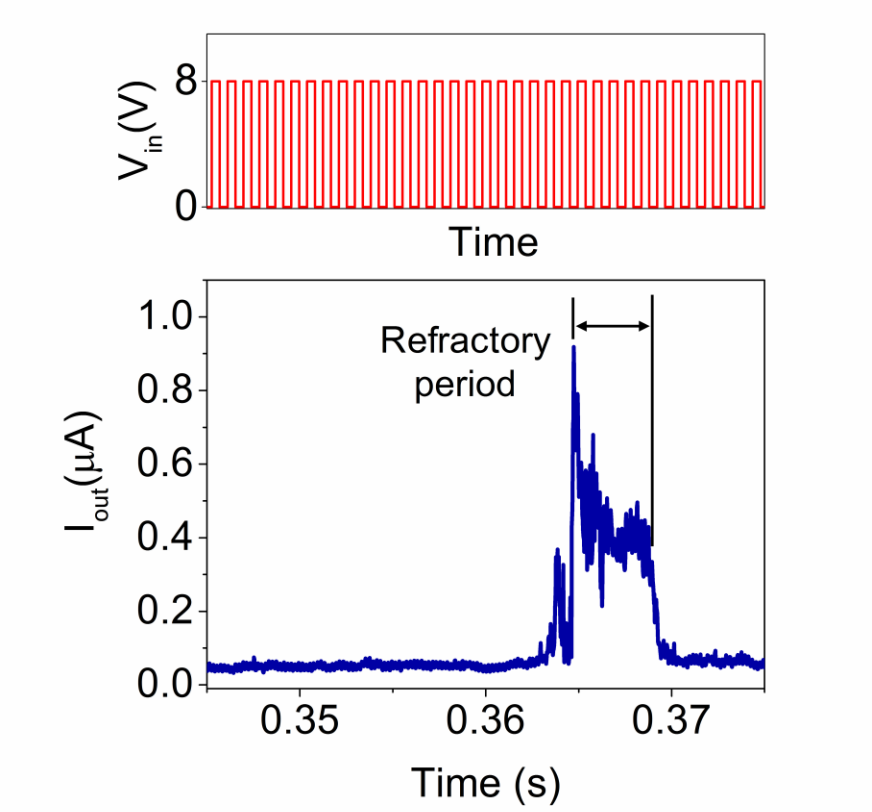

Figure 38. Output spike of the artificial neuron showing the refractory period along with the representative 8 V input pulses.

4.3.1 Strength Modulated Frequency Response

Another key characteristic of a biological neuron is that the frequency of spiking increases with increase in the strength of the input[17]. To emulate this behavior using the developed artificial neurons, a train of pulses with the same frequency 5 kHz (T_{on} = 100 µs) but two different amplitudes are applied to the v-MoS_2/graphene neurons. It is clearly seen from Figure 39 that during the same time period, the spiking frequency increases as the input amplitude is increased. On application of input pulses of 7.5V to the circuit, a potential drop across R_0 occurs leading to a voltage of ~4V at the node A and a single output current spike is observed. On the other hand, increasing the amplitude of the input pulses to 8.5 V, three different spikes in the same time period are observed. This behavior arises due to the varying capacitor charging time under different input amplitude conditions. Hence, the input strength modulated frequency dependence characteristics can be emulated by the developed v-MoS_2/graphene artificial neurons.

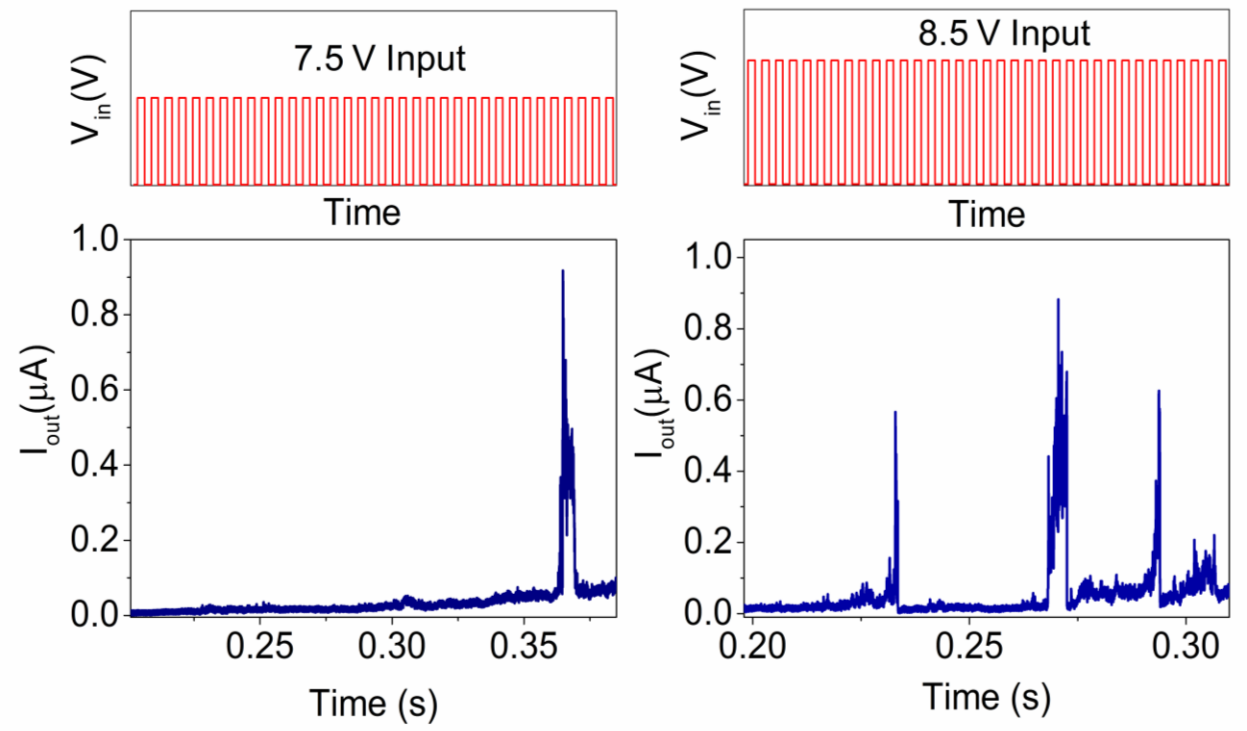

Figure 39. The TSM artificial neuron showing a strength modulated frequency at two different input pulse of amplitude 7.5 V and 8.5 V.

4.3.2 Stochastic Switching Behavior

We studied the DC characteristics of the TSM for over 40 cycles to shed light on the nature of the switching voltages. It is observed that the device retained the abrupt transition from the HRS to the LRS over this period as shown in Figure 40. The threshold voltage at which the device switches from the HRS to the LRS (V_1) and from the LRS to the HRS (V_2) are plotted over the 40 cycles shown in Figure 41.

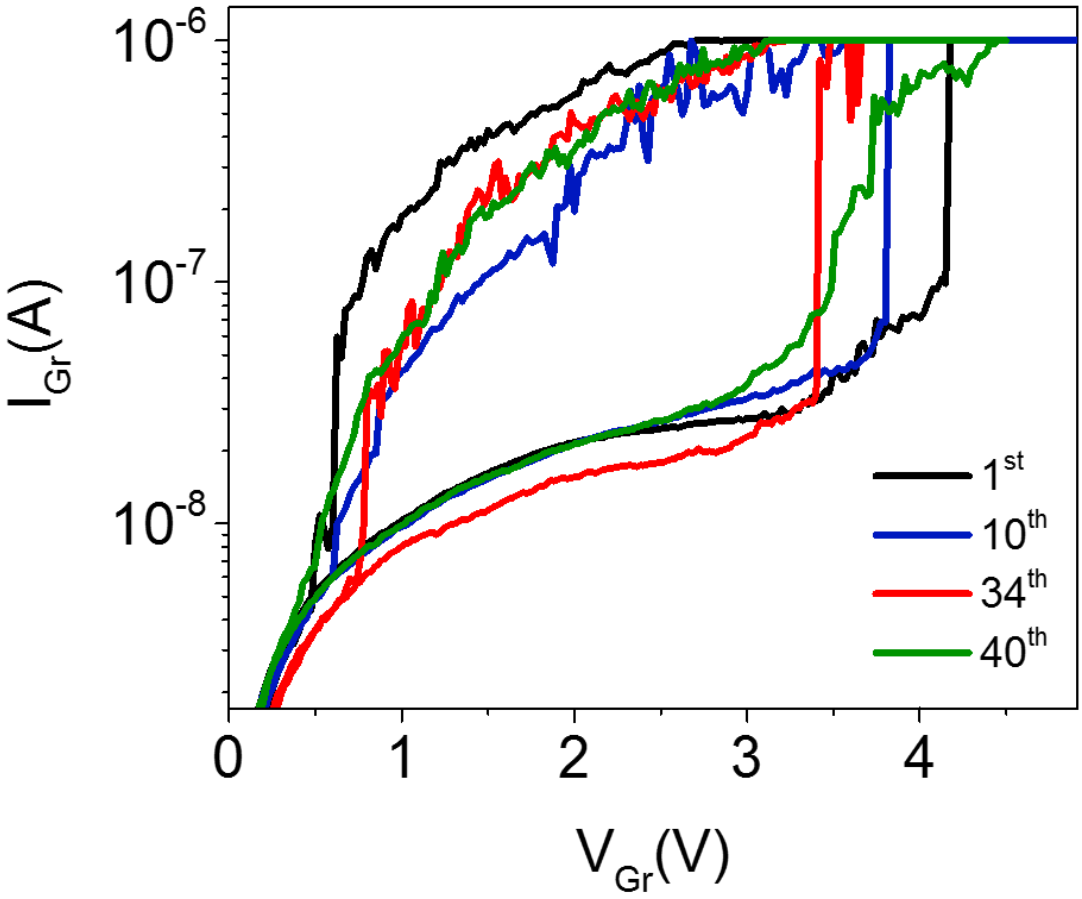

Figure 40. I-V characteristics of v-MoS_2/Graphene device over 40 cycles.

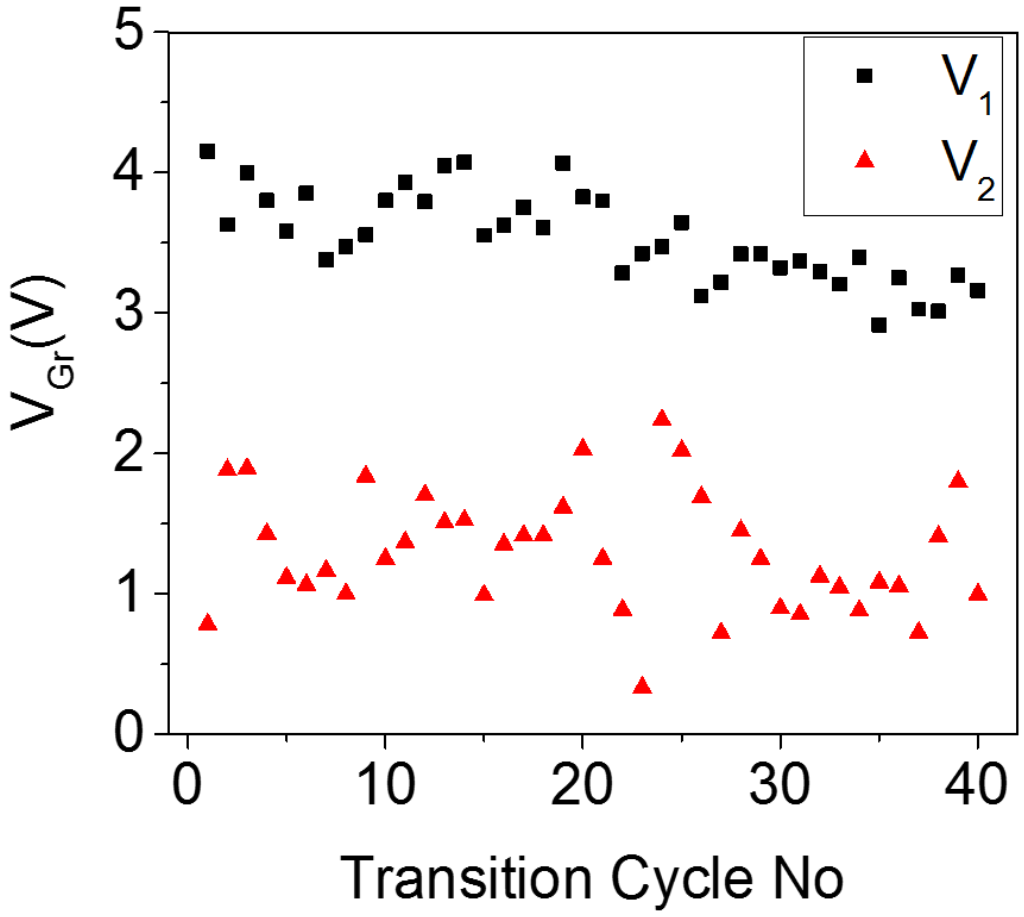

Figure 41. Variation of V_1 and V_2 over 40 cycles.

It is evident from Figure 42 that the window between V_1 and V_2 is maintained over the cycling period. Also, it is observed that V_1 and V_2 are completely probabilistic in nature and follow a stochastic distribution. Figure 43 shows the cumulative distribution function for the switching probability of the v-MoS_2/graphene TSM, which, in turn, produces the neuron spiking probability. Additionally, the stochastic switching behavior of the v-MoS_2/graphene TSM originating from device level stochasticity makes these probabilistic spiking neurons viable for

applications in the field of hardware security, such as Random Number Generators (RNGs). [32, 33]

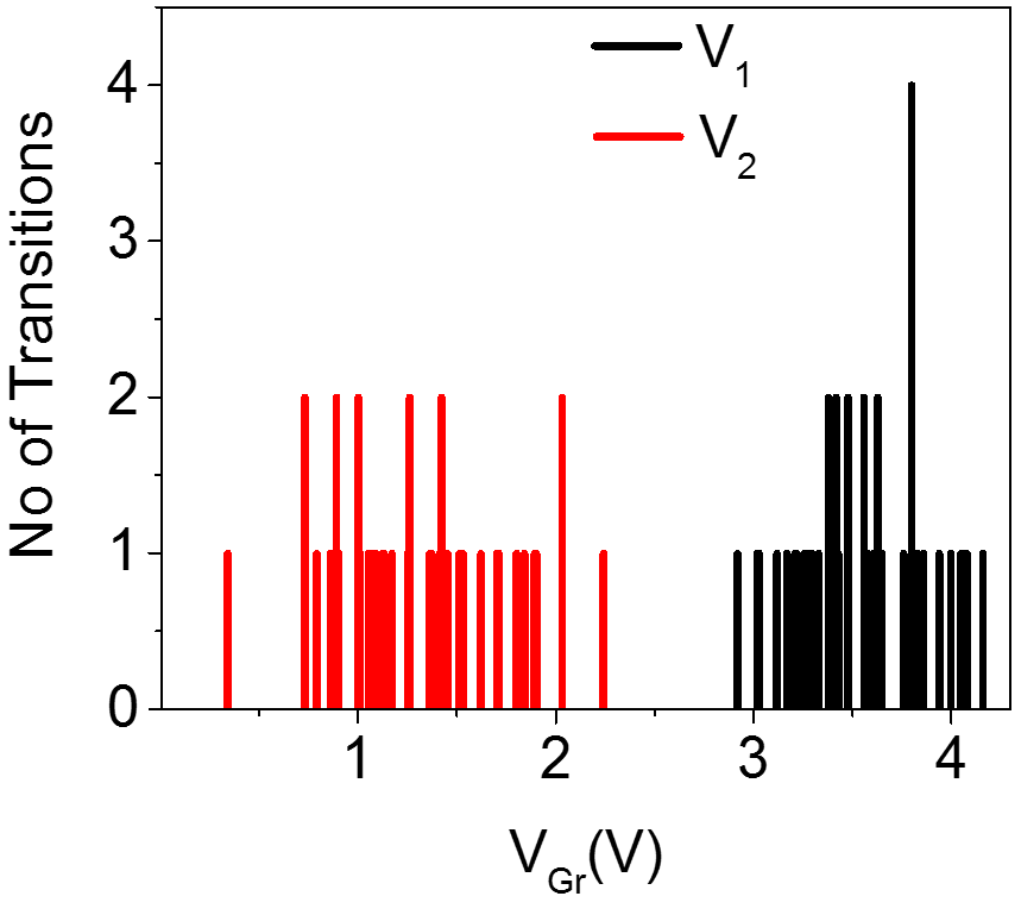

Figure 42. Number of HRS-LRS and LRS-HRS transitions corresponding to a particular V_1 and V_2, respectively.

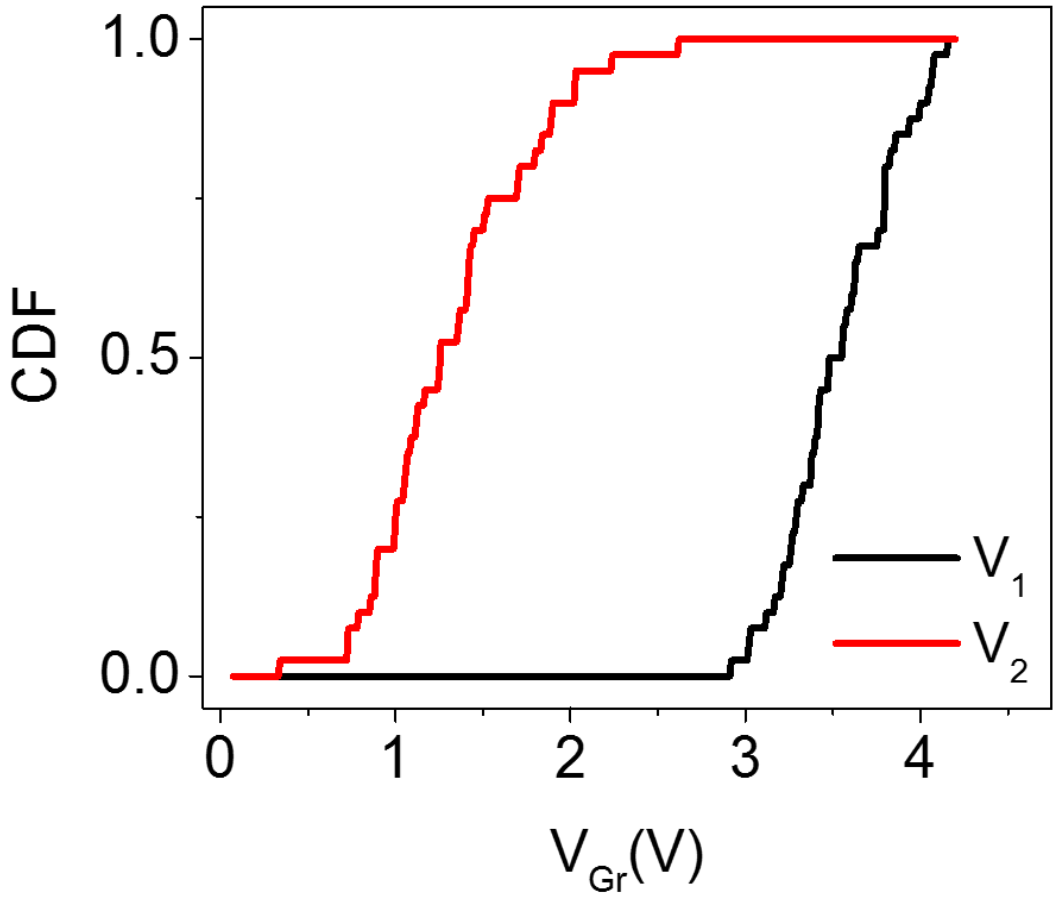

Figure 43. Cumulative distribution function of V_1 and V_2.

CHAPTER 5 : CONCLUSION

In summary, we have demonstrated a novel all 2D materials based TSM comprising of v-MoS_2 layers grown on a monolayer graphene template. The device mimics the critical characteristics of a biological neuron via the volatile resistive threshold switching behavior. These devices can be realized over a large area, and offers excellent offers excellent scalability which can be seamlessly integrated with the existing technologies. The developed MoS_2/graphene based IF artificial neuron exhibits the key behaviors of a biological neuron which include an all or nothing spiking, threshold driven spiking of the action potential, the post-firing refractory period of a neuron and the strength modulated frequency response. These properties coupled with the stochastic threshold switching behavior mediated by oxygen ion migration along the vertical grains of MoS_2 makes these artificial neurons viable for applications in real time computing systems based on event spiking such as pattern recognition, neuromorphic vision sensors, and hardware security.

We also studied the gate tunable IMT characteristics in 1T-TaS_2 using back gate SiO_2 as dielectric and realized an integrated device structure using 1T-TaS_2 which showed promising gate tunable characteristics using the Ta_2O_5 as the dielectric.

5.1 Future Scope

The developed v-MoS_2/graphene TSM artificial neuron could be a strong contender for future generation of electronics. An easily patternable vertical structure is shown in Figure 44 which can be adopted by designing the appropriate masks. The switching mechanism in v-MoS_2

can be studied in detail with the help of CAFM and TEM characterizations. These further studies can lead to increase in the current capacity of the neuron and hence, open a plethora of other applications for these artificial neurons. They can potentially be scaled down to nanometer scale cross bar structures and can even be realized on a flexible platform. Also, realizing synaptic behavior from such material system will allow heterogenous integration of the artificial neuron and synapse on the same chip for neuromorphic computing. These devices could be used to accomplish complex pattern recognition tasks.

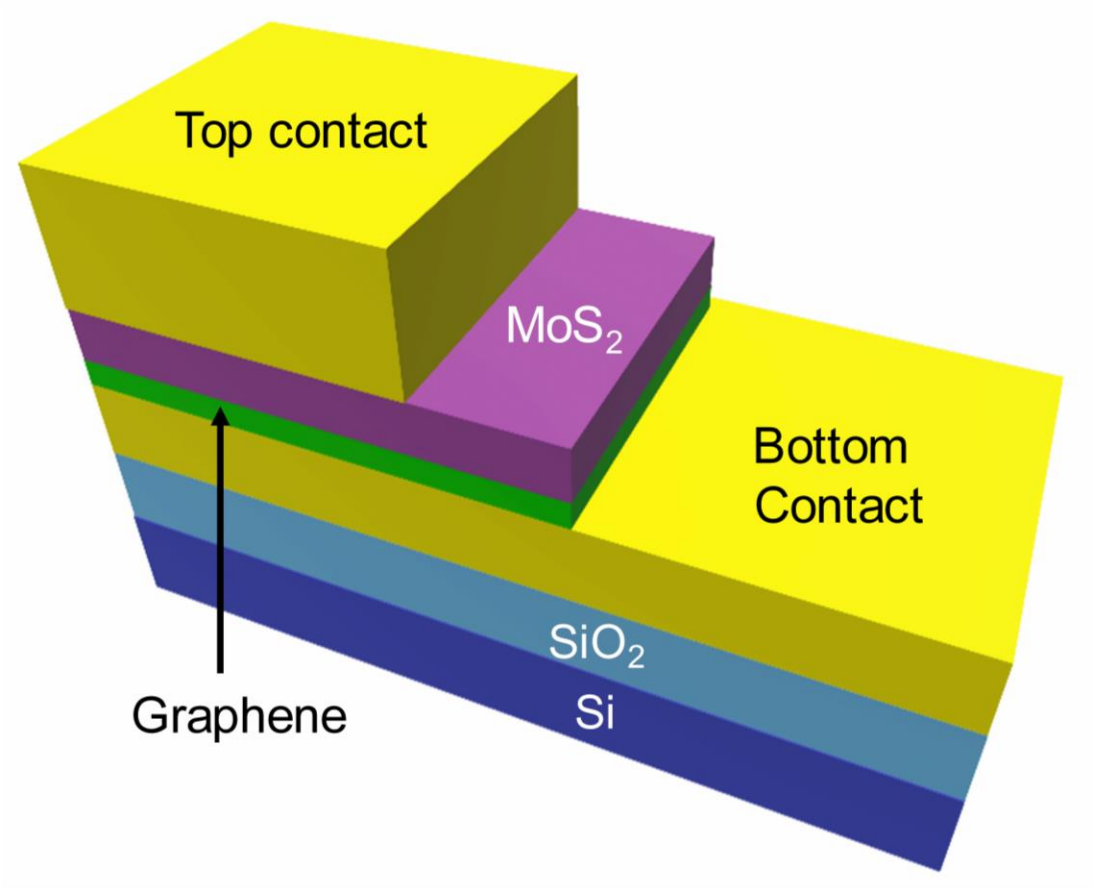

Figure 44. A complete vertical structure for the MoS_2/graphene device

LIST OF REFERENCES

[1] Jaiswal, A., et al., *Proposal for a Leaky-Integrate-Fire Spiking Neuron Based on Magnetoelectric Switching of Ferromagnets.* IEEE Transactions on Electron Devices, 2017. **64**(4): p. 1818-1824.

[2] 2D MaterialsBean, B.P., *The action potential in mammalian central neurons.* Nature Reviews Neuroscience, 2007. **8**(6): p. 451.

[3] Dayan, P. and L.F. Abbott, *Theoretical neuroscience, vol. 806*. 2001, Cambridge, MA: MIT Press.

[4] Lin, J., et al. *Low-voltage artificial neuron using feedback engineered insulator-to-metal-transition devices*. in *IEEE International Electron Devices Meeting (IEDM), 2016* 2016. IEEE.

[5] Vreeken, J., *Spiking neural networks, an introduction*. 2003, Utrecht University: Information and Computing Sciences.

[6] Tavanaei, A., et al., *Deep Learning in Spiking Neural Networks.* arXiv preprint arXiv:1804.08150, 2018.

[7] Prezioso, M., et al., *Training and operation of an integrated neuromorphic network based on metal-oxide memristors.* Nature, 2015. **521**(7550): p. 61.

[8] Tian, H., et al., *A novel artificial synapse with dual modes using bilayer graphene as the bottom electrode.* Nanoscale, 2017. **9**(27): p. 9275-9283.

[9] Seo, J.-s., et al. *A 45nm CMOS neuromorphic chip with a scalable architecture for learning in networks of spiking neurons*. in *IEEE Custom Integrated Circuits Conference (CICC), 2011* 2011. IEEE.

[10] Indiveri, G., E. Chicca, and R. Douglas, *A VLSI array of low-power spiking neurons and bistable synapses with spike-timing dependent plasticity.* IEEE transactions on neural networks, 2006. **17**(1): p. 211-221.

[11] Indiveri, G., et al., *Neuromorphic silicon neuron circuits.* Frontiers in neuroscience, 2011. **5**: p. 73.

[12] Douglas, R.J. and M.A. Mahowald, *Silicon neuron*. 1997, Google Patents.

[13] Jerry, M., et al. *Phase transition oxide neuron for spiking neural networks*. in *74th Annual Device Research Conference (DRC), 2016* 2016. IEEE.

[14] Pickett, M.D., G. Medeiros-Ribeiro, and R.S. Williams, *A scalable neuristor built with Mott memristors.* Nature materials, 2013. **12**(2): p. 114.

[15] Tuma, T., et al., *Stochastic phase-change neurons.* Nature nanotechnology, 2016. **11**(8): p. 693.

[16] Chen, P.-Y., et al. *Compact oscillation neuron exploiting metal-insulator-transition for neuromorphic computing*. in *Proceedings of the 35th International Conference on Computer-Aided Design*. 2016. ACM.

[17] Zhang, X., et al., *An Artificial Neuron Based on a Threshold Switching Memristor.* IEEE Electron Device Letters, 2018. **39**(2): p. 308-311.

[18] Fiori, G., et al., *Electronics based on two-dimensional materials.* Nature nanotechnology, 2014. **9**(10): p. 768.

[19] Chhowalla, M., D. Jena, and H. Zhang, *Two-dimensional semiconductors for transistors.* Nature Reviews Materials, 2016. **1**(11): p. 16052.

[20] Sangwan, V.K., et al., *Gate-tunable memristive phenomena mediated by grain boundaries in single-layer MoS 2.* Nature nanotechnology, 2015. **10**(5): p. 403.

[21] Dev, D., et al., *High quality gate dielectric/MoS2 interfaces probed by the conductance method.* Applied Physics Letters, 2018. **112**(23): p. 232101.

[22] Zheng, S., et al., *Room-temperature electrically driven phase transition of two-dimensional 1T-TaS 2 layers.* Nanoscale, 2017. **9**(7): p. 2436-2441.

[23] Hollander, M.J., et al., *Electrically driven reversible insulator–metal phase transition in 1T-TaS2.* Nano letters, 2015. **15**(3): p. 1861-1866.

[24] Hirata, T. and F. Ohuchi, *Temperature dependence of the Raman spectra of 1T-TaS2.* Solid state communications, 2001. **117**(6): p. 361-364.

[25] Yu, Y., et al., *Gate-tunable phase transitions in thin flakes of 1T-TaS 2.* Nature nanotechnology, 2015. **10**(3): p. 270.

[26] Chamlagain, B., et al., *Thermally oxidized 2D TaS2 as a high-κ gate dielectric for MoS2 field-effect transistors.* 2D Materials, 2017. **4**(3): p. 031002.

[27] Chan, J., et al., *Reducing extrinsic performance-limiting factors in graphene grown by chemical vapor deposition.* ACS nano, 2012. **6**(4): p. 3224-3229.

[28] Li, H., et al., *From bulk to monolayer MoS2: evolution of Raman scattering.* Advanced Functional Materials, 2012. **22**(7): p. 1385-1390.

[29] Childres, I., et al., *Raman spectroscopy of graphene and related materials.* New developments in photon and materials research, 2013. **1**.

[30] Joiner, C.A., et al., *Graphene-Molybdenum Disulfide-Graphene Tunneling Junctions with Large-Area Synthesized Materials.* ACS applied materials & interfaces, 2016. **8**(13): p. 8702-8709.

[31] Choudhary, N., et al., *Strain-Driven and Layer-Number-Dependent Crossover of Growth Mode in van der Waals Heterostructures: 2D/2D Layer-By-Layer Horizontal Epitaxy to 2D/3D Vertical Reorientation.* Advanced Materials Interfaces, 2018: p. 1800382.

[32] Jerry, M., et al. *A random number generator based on insulator-to-metal electronic phase transitions*. in *75th Annual Device Research Conference (DRC), 2017* 2017. IEEE.

[33] Jerry, M., et al. *Ultra-low power probabilistic IMT neurons for stochastic sampling machines*. in *2017 Symposium on VLSI Circuits*. 2017. IEEE.